UNICO I+D Project
6G-INTEGRATION-01

6G-INTEGRATION-01-E10

EBBM Design

Abstract

This document presents the research and pre-design of the Building Block Module of an Electronically Steerable Antenna (ESA Building Block Module or EBBM) for the ground segment of low orbit satellite constellations (LEO). This activity contributes to the integration of the B5G and NTN networks within the 6G-INTEGRATION project. The EBBM incorporates beamforming techniques and represents the starting point for an antenna that can be operational in a 3GPP environment (Release 17 and later) in which the NTN network is integrated into the 5G NG-RAN.

Financiado por la Unión Europea NextGenerationEU
GOBIERNO DE ESPAÑA MINISTERIO DE ASUNTOS ECONÓMICOS Y TRANSFORMACIÓN DIGITAL SECRETARÍA DE ESTADO DE TELECOMUNICACIONES E INFRAESTRUCTURAS DIGITALES
Plan de Recuperación, Transformación y Resiliencia
UNICO I+D

Document properties

Document number	6G-INTEGRATION-01-E10
Document title	EBBM Design
Document responsible	Daniel Segovia (UC3M)
Document editor	Jaime Suarez (INSTER)
Editorial team	Jaime Suarez (INSTER)
Target dissemination level	Public
Status of the document	Final
Version	1.0
Delivery date	28-02-2024
Actual delivery date	28-02-2024

Production properties

Reviewers

Disclaimer

This document has been produced in the context of the 6G-INTEGRATION-01 Project. The research leading to these results has received funding from the Spanish Ministry of Economic Affairs and Digital Transformation and the European Union-NextGenerationEU through the UNICO 5G I+D programme.

All information in this document is provided “as is" and no guarantee or warranty is given that the information is fit for any particular purpose. The user thereof uses the information at its sole risk and liability.

Contents

List of Figures

List of Tables

List of Acronyms

EBBM: ESA Building Block Module

EIRP: Equivalent Isotropic Radiated Power

ESA: Electronic Steerable Antenna

G/T: Gain over Temperature

GND: Ground

IC: Integrated Circuit

LEO: Low Earth Orbit

LHCP: Left-Hand Circular Polarization

NTN: Non-Terrestrial Network

PCB: Printed Circuit Board

RF: RadioFrequency

RHCP: Right-Hand Circular Polarization

RX: Reception

SLL: Side Lobe Level

TX: Transmission

Resumen Ejecutivo

Este documento expone el prediseño del EBBM de un terminal terrestre para las constelaciones satelitales de baja órbita emergentes capaz de integrarse con la arquitectura celular B5G. El prediseño propuesto incorpora soluciones de RF innovadoras que optimizan el rendimiento electromagnético de la apertura al tiempo que reducen sus dimensiones y peso. Asimismo, se explotan técnicas avanzadas de conformado de haz electrónico para realizar el seguimiento de los satélites LEO a una velocidad muy superior a la permitida por los sistemas mecánicos.

Siguiendo los principios de flexibilidad y escalabilidad, la agrupación de varios módulos como el presentado en este entregable confeccionará la antena LEO que finalmente pueda operar en un entorno 3GPP en el que las redes no terrestres se integren en la 5G NG-RAN.

Los principales resultados contenidos en este entregable son:

- Descripción de la topología de los elementos radiantes
- Resultados de simulación del elemento radiante de recepción
- Resultados de simulación del elemento radiante de transmisión
- Descripción de la apertura radiante relativa al módulo EBBM (ESA Building Block Module)
- Resultados de simulación de la apertura radiante del módulo EBBM de recepción
- Resultados de simulación de la apertura radiante del módulo EBBM de transmisión
- Descripción de las redes de alimentación de RF relativas al módulo EBBM
- Resultados de simulación del combinador individual para la red de alimentación de RF de recepción
- Resultados de simulación de la red de alimentación de RF del módulo EBBM de recepción
- Resultados de simulación del divisor individual para la red de alimentación de RF de transmisión
- Resultados de simulación de la red de alimentación de RF del módulo EBBM de transmisión

El resto del documento está redactado en inglés, de cara a maximizar el impacto del trabajo realizado en este proyecto.

Executive Summary

This document outlines the EBBM pre-design of a ground terminal for emerging low-orbit satellite constellations that can be integrated within the B5G architecture. The proposed pre-design incorporates innovative RF solutions that optimize the electromagnetic performance of the aperture while reducing its dimensions and weight. Additionally, electronic beamforming techniques are exploited to track LEO satellites at a much higher speed than mechanical systems, and avoiding the well-known keyhole problem.

The grouping of several EBBM modules as the depicted in this deliverable allows creating an optimal LEO antenna able to operate in a 3GPP environment in which the NTN network is integrated into the 5G NG-RAN.

In particular, the main results contained in this deliverable are:

- Topology description of the individual radiating elements
- Reception radiating element simulation results
- Transmission radiating element simulation results
- Description of the ESA Building Block Module (EBBM) radiating aperture
- Reception EBBM radiating aperture simulation results
- Transmission EBBM radiating aperture simulation results
- Description of EBBM RF feeding networks
- Simulation results of the single combiner for the reception feeding network
- Reception EBBM RF feeding network simulation results
- Simulation results of the single splitter for the transmission RF feeding network
- Transmission EBBM RF feeding network simulation results

1. Introduction

6G-INTEGRATION aims to integrate B5G and NTN networks. From the user segment point of view, a low-profile satellite communications terminal is required. The terminal will provide global, high-bandwidth, low-latency connectivity through a low-orbit constellation, and must consist of a flat Electronically Steerable Antenna, whose beam is pointed to the LEO satellites automatically and in real time using beamforming techniques. The terminal must be designed in accordance with the principles of sustainability, reliability, and optimization of size, weight, consumption and cost.

The starting point for the implementation of the mentioned terminal is the design of an EBBM. This EBBM represents the minimum constituent module from which a larger radiant aperture can be generated optimizing the necessary computational cost. The pre-design of this EBBM is the task addressed in this deliverable.

The document has been structured into 4 main chapters:

Chapter 2 presents the pre-design of the individual radiating element, which constitutes the basic element of the EBBM. Based on the specifications that the individual element must satisfy so that the EBBM and the complete antenna can operate in the emerging LEO satellite constellations, the chosen topology is exposed (such as the geometry of the microstrip patch or the type and number of feeds), and the results obtained in the electromagnetic simulations are shown.

The construction of the EBBM radiating aperture from the individual radiating element is addressed in Chapter 3. Advanced techniques such as the use of 2x2 synchronous sub-arrays for the construction of the EBBM are described. The size of the array of radiating elements that form the EBBM is also specified and, finally, the performance of the EBBM that has been obtained through the different electromagnetic simulations is presented.

Chapter 4 addresses the pre-design of the EBBM RF feeding networks, from the single combiner/splitter to the complete networks. The chosen combiner/splitter topology is presented, and the results obtained in the electromagnetic simulations are shown. Based on the individual combiner and splitter, the reception and transmission EBBM RF feeding networks are generated and simulated.

Chapter 5 includes the summary and the conclusions.

2. Simulation of the Radiating Element

The study of the individual radiating element, as well as the simulation results obtained, are collected in this section. The individual radiating element has been designed according to the preliminary requirements of the LEO user terminal. These requirements, which are referred to the whole user terminal Electronic Steerable Antenna, are collected in the following table.

ID	NAME	VALUE	COMMENTS
RF-1	Frequency range	RX: 10.7 – 12.7 GHz TX: 14.0 – 14.5 GHz	
RF-2	Polarization	RX: RHCP TX: LHCP	
RF-3	Scanning range	Azimuth: 0 – 360º Elevation: 40 – 90º	
RF-4	EIRP @Plinear	≥ 35 dBW	For the whole frequency and scanning range
RF-5	G/T	≥ 7 dB/K	For the whole frequency and scanning range
RF-6	Axial Ratio	≤ 2.5 dB	For the whole frequency and scanning range
TR-1	Steering	Electronic Steering	

TABLE 1: PRELIMINARY REQUIREMENTS OF THE LEO USER TERMINAL

Since an electronic steerable antenna is required, but there are no requirements regarding multi-beam and/or advanced processing signal techniques (direction-of-arrival estimation, beacon receiver, etc.), an analog beamforming architecture is proposed [1], [2]. Compared with hybrid and digital beamforming architectures, the analog beamforming architecture presents advantages in terms of size, power consumption, power dissipation, complexity, and cost [3], [4], [5].

For simplicity, and looking into a future massive production, the analog beamforming architecture will be implemented in Printed Circuit Board (PCB) technology. The bottom layer of the PCB will contain the beamforming integrated circuits (ICs) and the RF feeding network, while the top layers will be dedicated to the radiating elements. Other internal layers in between will be used for power supply and digital signals distribution.

Following the same radiating element topology, two different radiating elements are designed: one for reception (RX), and another for transmission (TX). The selected radiating element topology is depicted in the following figure, where substrate layers have been omitted. This topology uses stacked patches, where the upper patch (parasitic patch) is fed by the coupling received from the lower patch. In turn, the lower patch (driven patch) is fed by a dual probe-feed. In the PCB technology, the dual probe-feed will be carried out by vias.

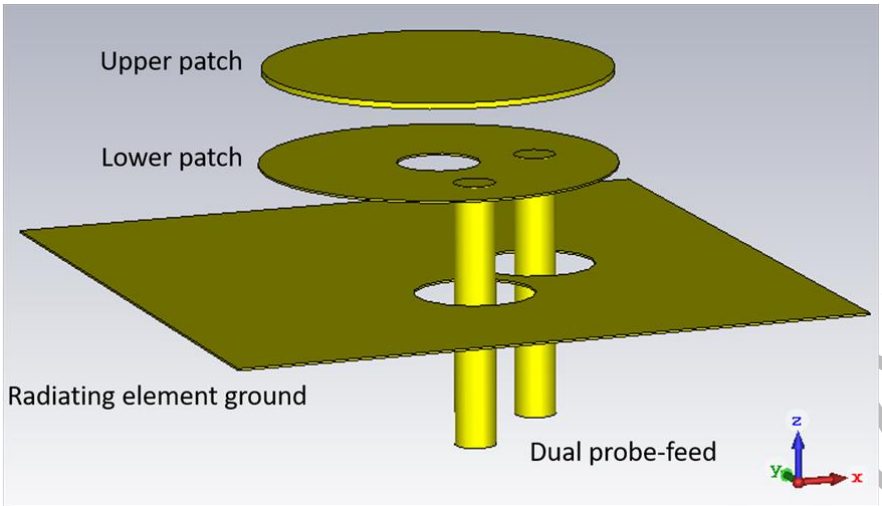

FIGURE 1: INDIVIDUAL RADIATING ELEMENT TOPOLOGY

Stacked patches are used to increase the radiating element bandwidth [6], [7], [8]. This is especially necessary in the RX radiating element, where the relative bandwidth is higher than 17%.

Dual feeding is a widely used feeding technique used for obtaining a circular polarization [9], [10]. Each radiating element is simultaneously fed in two orthogonal directions with equal amplitude and 90° phase-difference. In this way, two different modes are excited in the patch and the circular polarization is generated, to the right or to the left depending on the specific feed that is 90° out of phase.

Circular polarization could be also obtained by using a single feed and a different patch topology [11], [12], [13]. However, there is a specific reason for using two feeds. Typically, the EIRP of such an electronic steerable antenna is limited by the saturation output power of the beamforming ICs. By using dual feeding, it is possible to duplicate the power delivered to the antenna preserving the same radiating area. On the contrary, this complicates the power dissipation and integration tasks.

Since the dual feeding need to go from beamforming ICs (bottom layer) to radiating patches (top layer), vias that go through all the layers of the PCB are used. To reduce impedance mismatching, the core and prepreg substrate materials of the PCB have been selected to have similar radioelectric characteristics. The permittivity and loss tangent of both substrate materials are:

SUBSTRATE	ε_r @10GHz	tanδ @10GHz
Core	3.00	0.0023
Prepreg	2.94	0.0030

TABLE 2: PCB SUBSTRATE RADIOELECTRIC CHARACTERISTICS

Multiple discussions with manufacturers have been made to validate the usage of the previous materials, as well as to define the PCB stack-up of the radiating element. In Figure 2, the PCB stack-up is depicted. Please, note that height measurements are specified in mils in that figure.

The first four layers are reserved for the radiating element structure. L1 and L2 are reserved for upper and lower patches, while L4 is used as the radiating element ground. Layer L3, which is empty, is only included for manufacturing feasibility. Layers L5 and L7 are reserved for power and digital distribution, respectively. They are isolated by the L6 ground layer, following manufacturing recommendations. Finally, bottom layer L9 contains the RF feeding network, the beamforming ICs, and other required components.

As depicted, vias and microvias are used to interconnect the different layers. In addition, PCB backdrills between layers L1 and L2, and between layers L3 and L4, can be done by the manufacturer. This procedure allows to remove undesired copper of the vias, creating direct via connections from bottom to L2 (driven patches) and to L4 (radiating aperture GND).

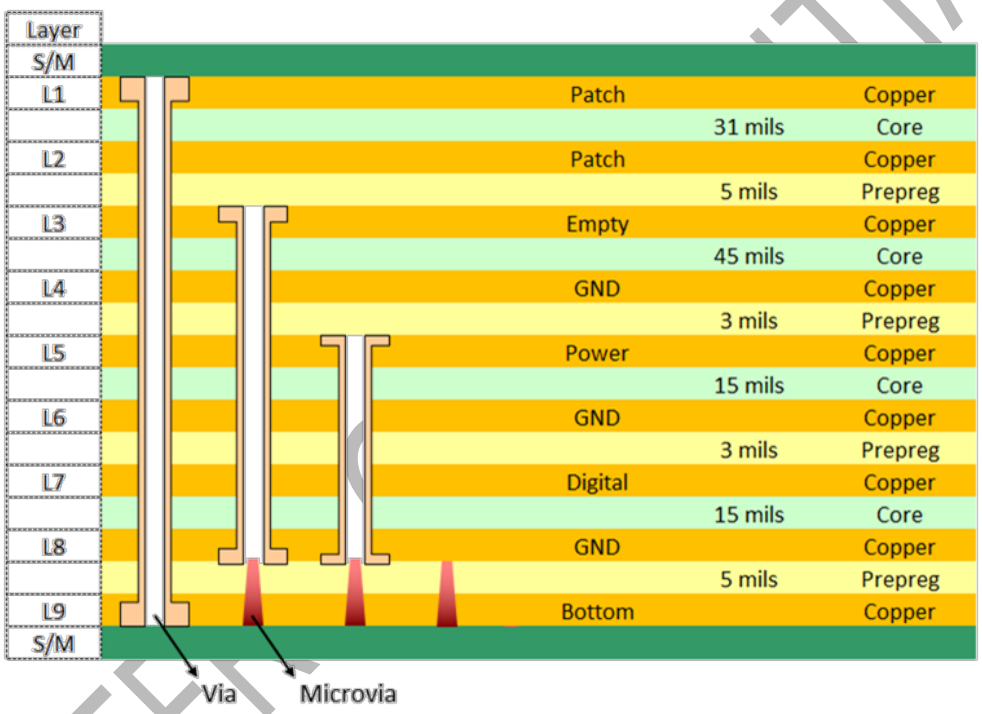

FIGURE 2: PCB STACK-UP OF THE RADIATING ELEMENT

The following figure shows the whole radiating element topology in PCB technology, configured in the radiofrequency simulation tool (CST Studio Suite). It includes the radiating element and all the intermediate layers that need to be crossed to reach the bottom layer.

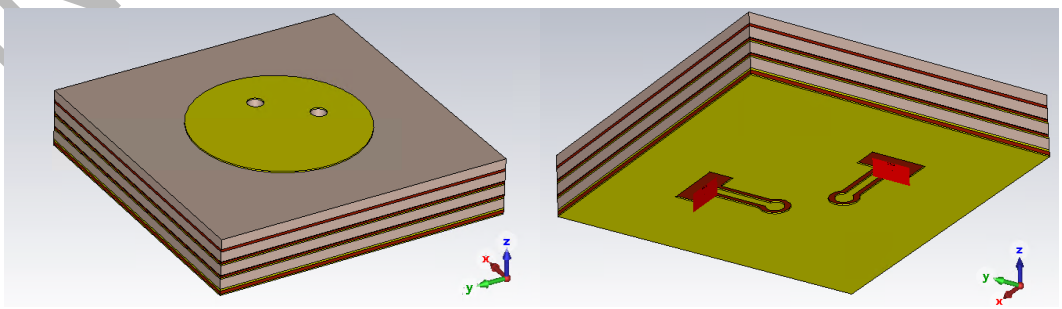

FIGURE 3: INDIVIDUAL RADIATING ELEMENT IN PCB TECHNOLOGY

The requirements that the individual RX and TX radiating elements must satisfy are collected in the following table. These requirements have been derived from the preliminary requirements of the LEO antenna (Table 1).

ID	NAME	VALUE	COMMENTS
RF-RE-1	Frequency range	RX: 10.7 – 12.7 GHz TX: 14.0 – 14.5 GHz	
RF-RE-2	Polarization	RX: RHCP TX: LHCP	
RF-RE-3	Gain	≥ 5 dBi	At boresight, for the whole frequency range
RF-RE-4	Axial Ratio	≤ 2 dB	At boresight, for the whole frequency range
RF-RE-5	3dB Beamwidth	≥ 85º	For the whole frequency range
RF-RE-6	Reflection coefficient (S1,1 and S2,2)	≤ -12 dB	For the whole frequency range
RF-RE-7	Coupling between antenna ports (S2,1 and S1,2)	≤ -18 dB	For the whole frequency range

TABLE 3: REQUIREMENTS FOR THE INDIVIDUAL RADIATING ELEMENTS

The different design parameters of the radiating element structure from Figure 3 have been optimized for both the reception and transmission working frequency bands and are detailed in Table 4. The simulation results obtained for the RX and the TX radiating elements are detailed in the following sub-sections.

DESIGN PARAMETER	RX RADIATING ELEMENT	TX RADIATING ELEMENT
Upper patch radius [mm]	3.690	3.168
Lower patch outer radius [mm]	3.790	3.118
Lower patch inner radius [mm]	0	0
Feeding point offset (from the patch center; both in X and Y axis) [mm]	2.150	1.550
Feeding probe radius [mm]	0.175	0.175
Feeding probe isolation radius at RF ground [mm]	0.510	0.510

TABLE 4: OPTIMIZED DESIGN PARAMETERS OF THE RECEPTION AND TRANSMISSION RADIATING ELEMENTS

2.1. RX radiating element simulation results

RX radiating element S-parameters are shown in Figure 4, while radiation and total efficiencies are depicted in Figure 5. Reflection coefficients S1,1 and S2,2 are lower than -12 dB for all the RX working frequencies, complying with the established requirement. In the same way, coupling between ports is lower than -18 dB.

Best performance is expected between 11 and 11.5 GHz, approximately. In fact, a very low difference between radiation efficiency and total efficiency can be seen in Figure 5 at 11.2 GHz. Worst total efficiency values are obtained at the lower and upper RX working frequencies.

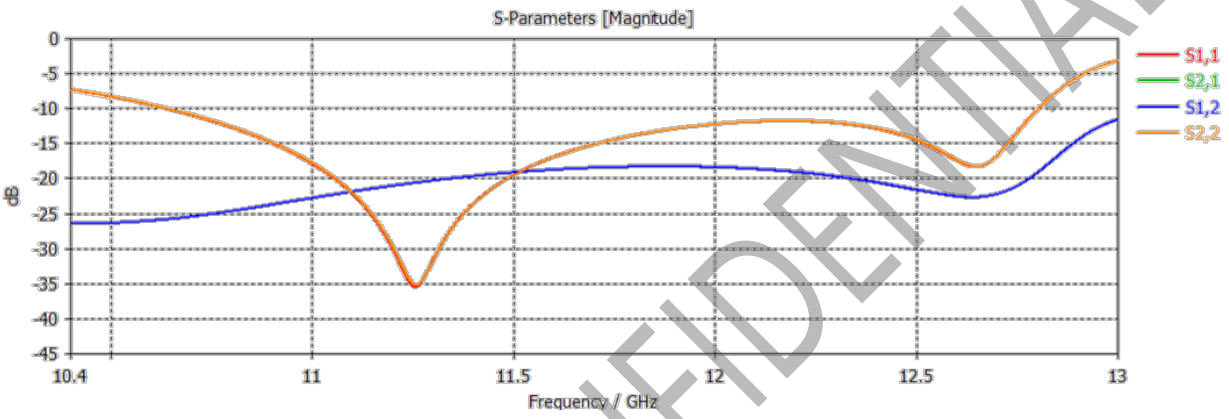

FIGURE 4: RX RADIATING ELEMENT: S-PARAMETERS

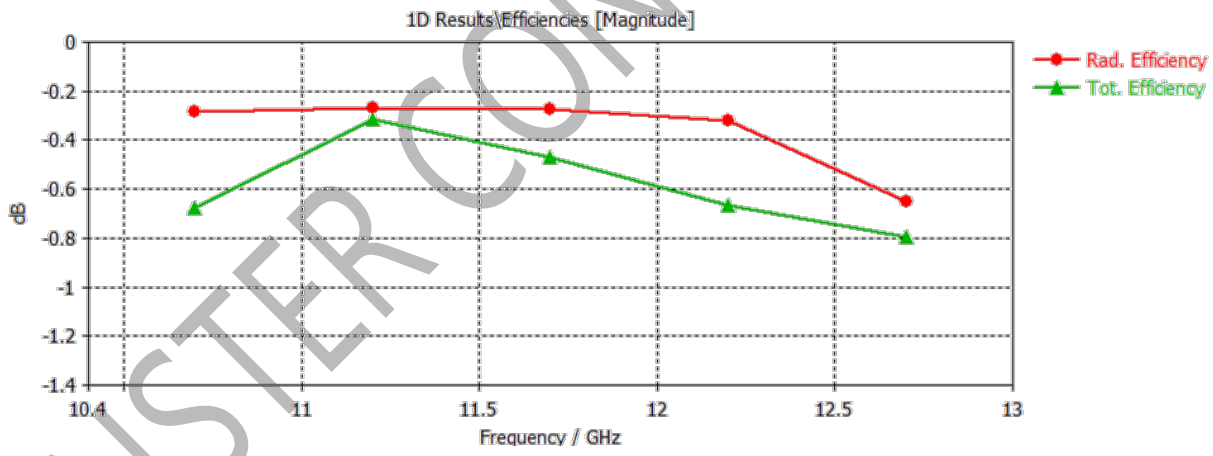

FIGURE 5: RX RADIATING ELEMENT: EFFICIENCY

The following figure presents the gain obtained for the RX radiating element at the lower, central, and upper RX working frequencies. In line with previous efficiency results, the gain obtained at the lower and upper frequencies are worse than the gain obtained at 11.7 GHz. Despite this, the gain values obtained are higher than 5 dBi, complying with the established requirement. The 3 dB beamwidth obtained is also higher than 85º.

A discrete pointing error can be observed in the radiation patterns, which are not completely centered at boresight (θ = 0º). This effect can be specially seen at 11.7 GHz, where the maximum gain is obtained at θ = 5º. However, the gain difference observed between θ = 0º and θ = 5º at 11.7

GHz is negligible: the 0.1dB beamwidth is higher than 16º. In addition, this pointing error is not expected to exist in the EBBM radiating aperture due to the specific grouping configuration that will be used. This specific array configuration will be described in Chapter 3.

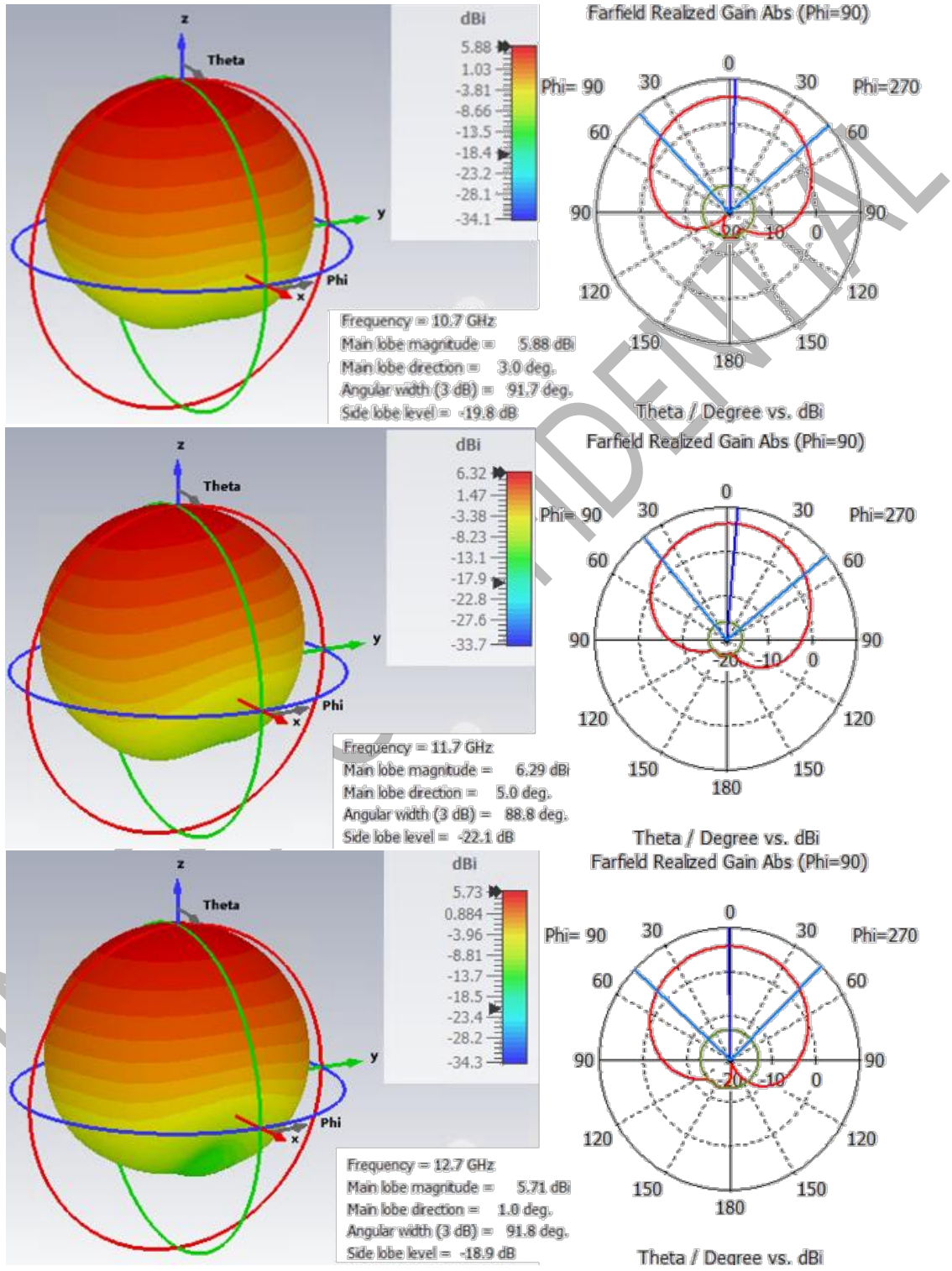

FIGURE 6: RX RADIATING ELEMENT: RADIATION PATTERN (GAIN)

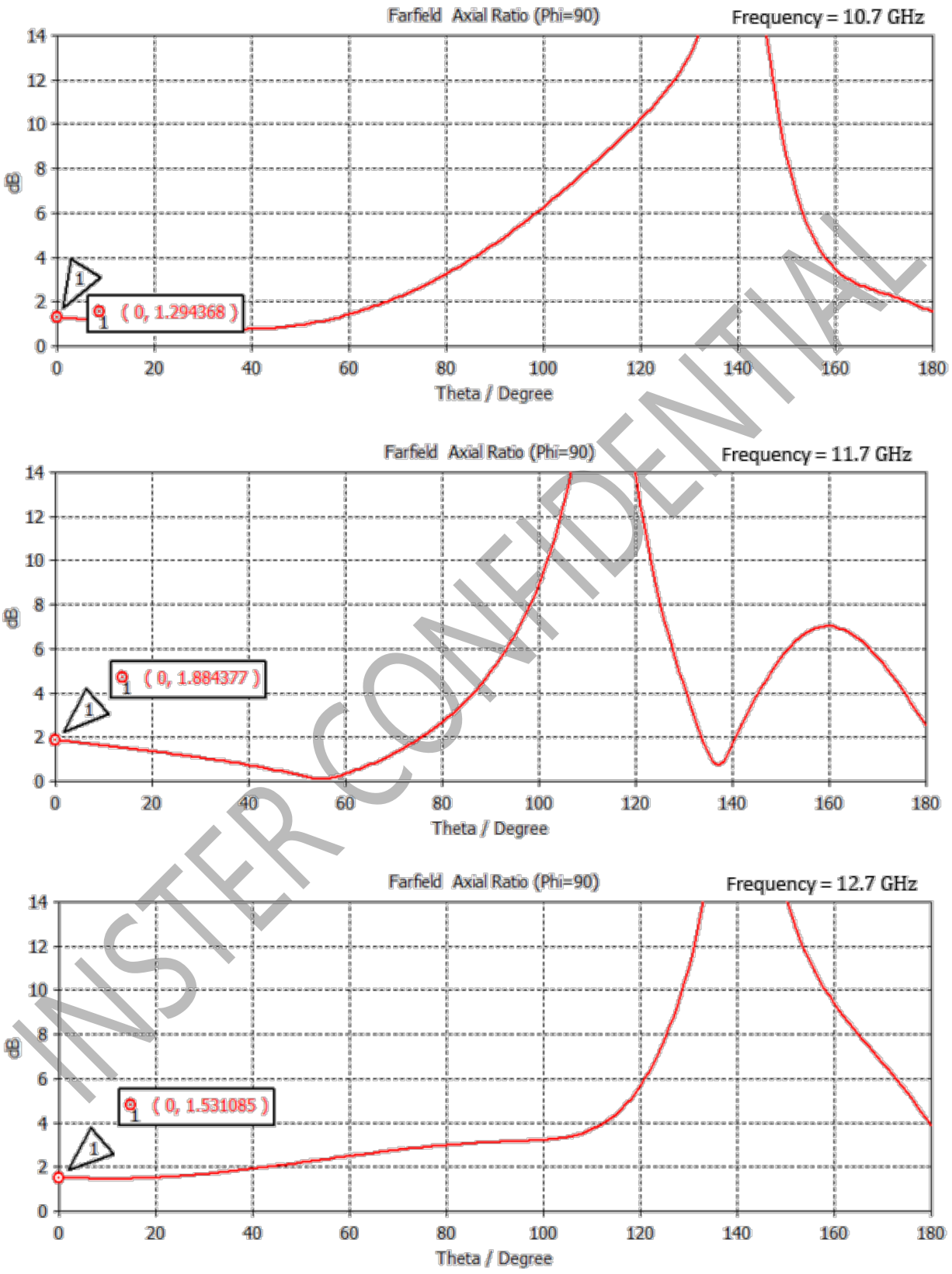

FIGURE 7: RX RADIATING ELEMENT: AXIAL RATIO AT 10.7, 11.7 AND 12.7GHZ

Previous figure shows the axial ratio results obtained at boresight for the lower, central, and upper RX working frequencies. Worst results are obtained for the 11.7 GHz central frequency, where the axial ratio is close to 2 dB. This parameter is expected to improve in the array configuration, since the directivity of the antenna will be higher. In addition, a sequential rotation architecture followed by a quadrature phase shifting correction will be applied, as explained in future sections of this document. This technique is expected to strengthen the desired circular polarization, reducing the axial ratio.

2.2. TX radiating element simulation results

TX radiating element S-parameters are depicted the following figure. Both the reflection coefficients and the coupling between ports are compliant with the established requirements. Better results than in the RX radiating element have been achieved. The main reason is that the TX radiating element requires a 3.5% relative bandwidth, easier to obtain than the 17% relative bandwidth required by the RX radiating element.

The best performance of the TX radiating element is obtained at the central frequency, where the reflection coefficient is lower than -25 dB, and the total efficiency of the patch approximately matches its radiation efficiency, as depicted in Figure 9.

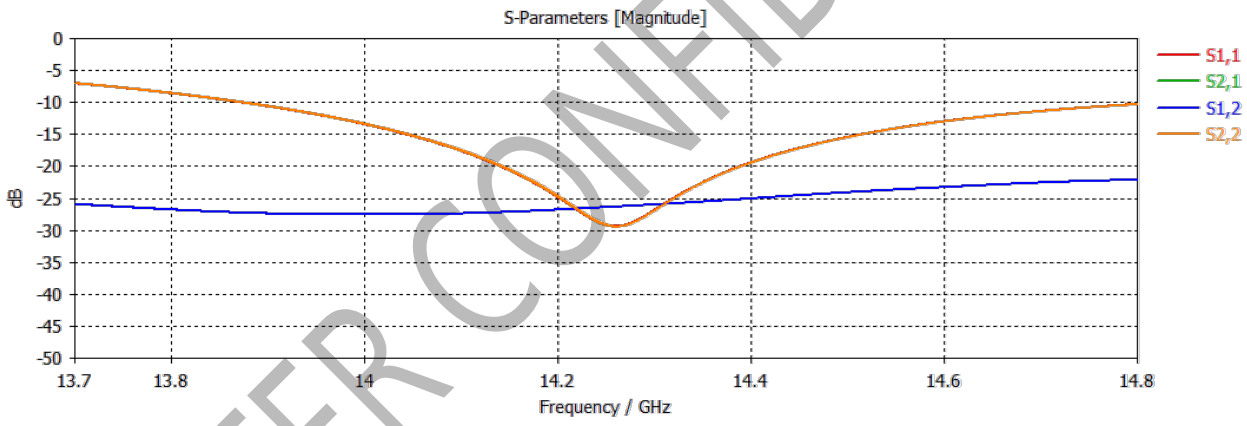

FIGURE 8: TX RADIATING ELEMENT: S-PARAMETERS

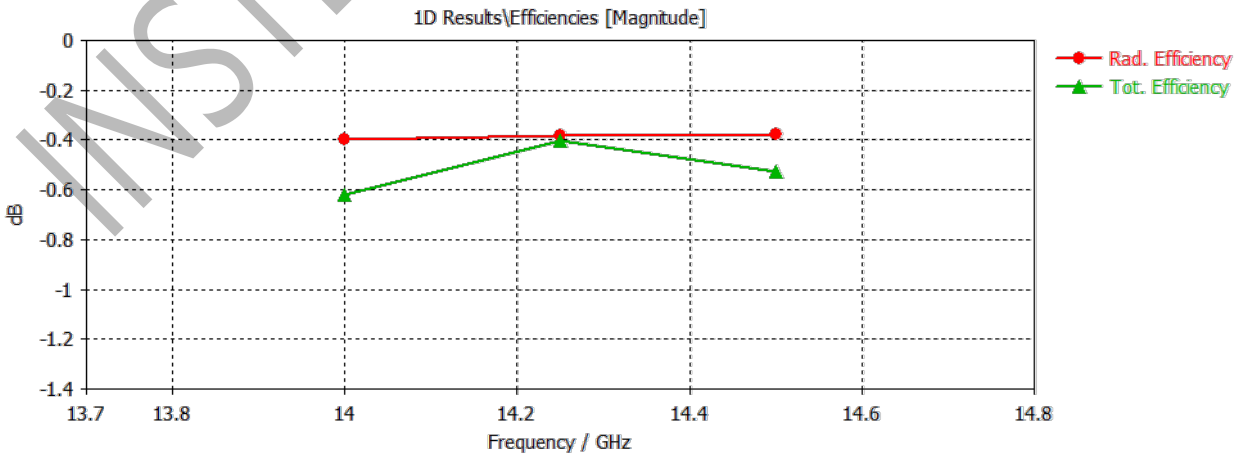

FIGURE 9: TX RADIATING ELEMENT: EFFICIENCY

The gain radiation patterns of the TX radiating element are presented in Figure 10, for the lower, central, and upper TX working frequencies. The gain values achieved at boresight are higher than 6 dBi, which is compliant with the individual radiating element gain requirement. The 3 dB beamwidth obtained is also higher than 85º.

Again, a small pointing error can be seen in the different radiation patterns presented, since they are not completely centered at boresight (θ = 0º). Nevertheless, the difference between the maximum gain and the boresight gain is negligible and is expected to disappear in the EBBM radiating aperture due to the specific array configuration used (Chapter 3).

The axial ratio results achieved at boresight for the lower, central, and upper TX working frequencies are shown in Figure 11. The worst result is obtained for the 14.5 GHz upper frequency. In this case, the axial ratio is lower than 1 dB, compliant with the individual radiating element axial ratio requirement. Again, the axial ratio is expected to improve in the array configuration due to the directivity increase and the sequential rotation technique.

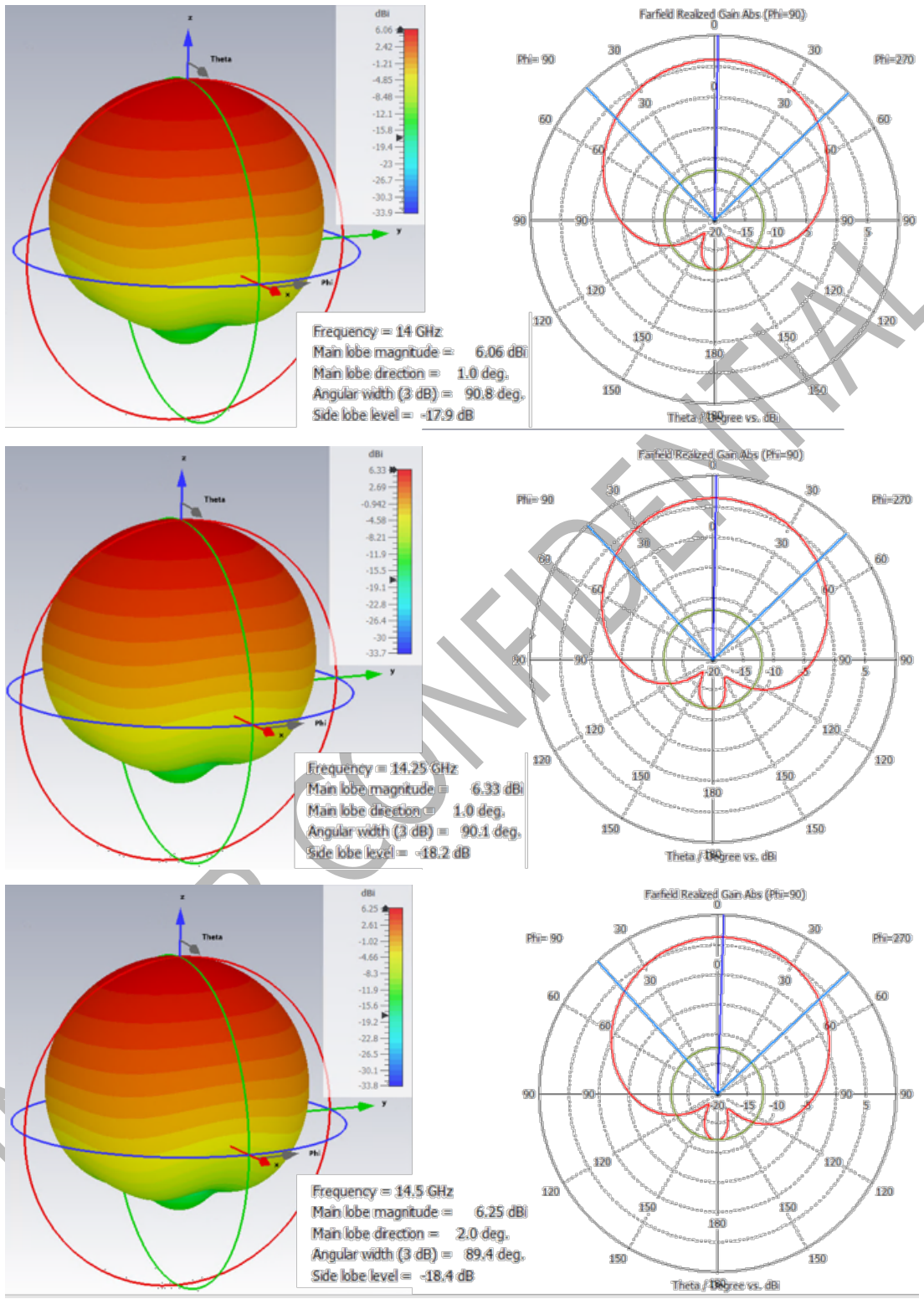

FIGURE 10: TX RADIATING ELEMENT: RADIATION PATTERN (GAIN)

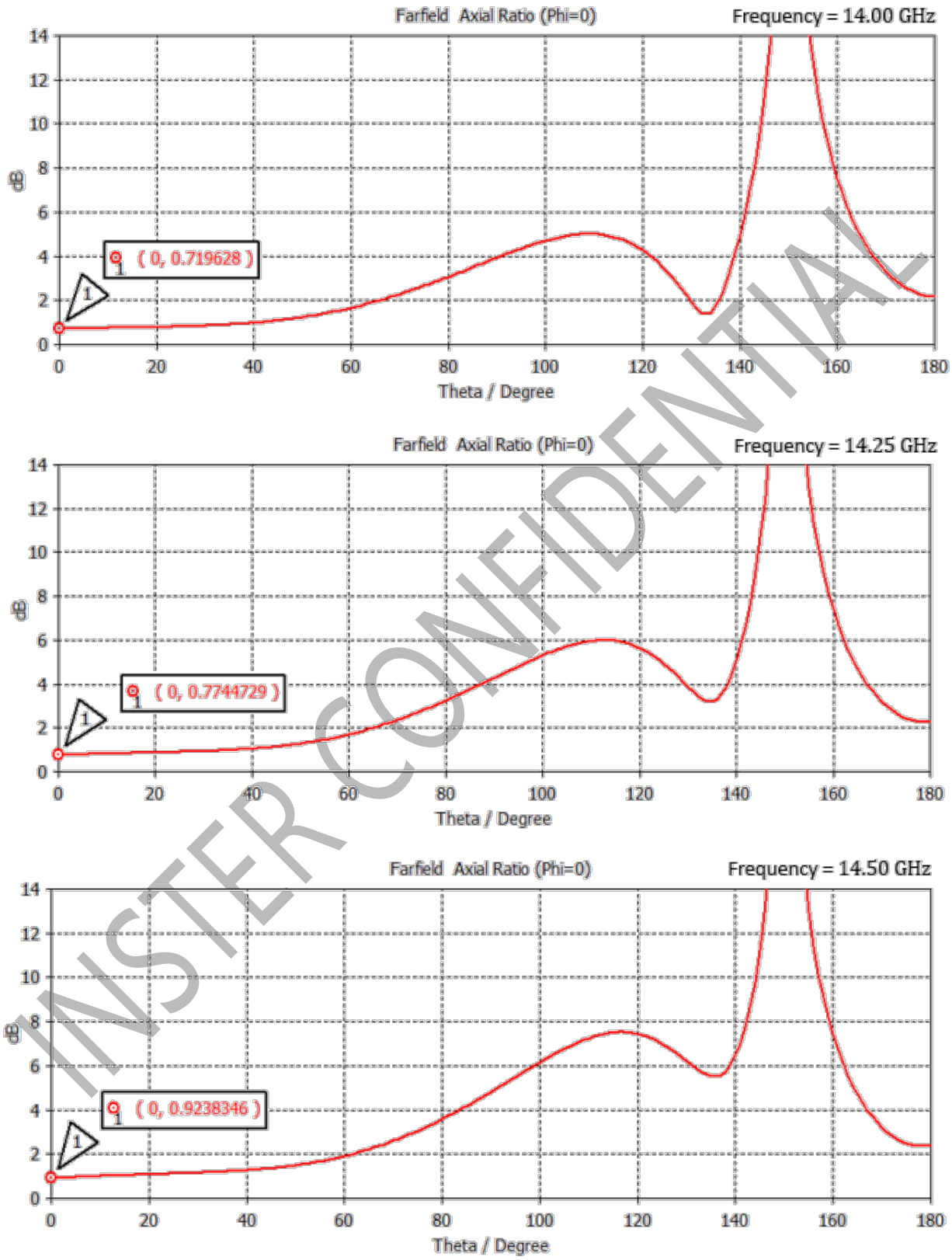

FIGURE 11: TX RADIATING ELEMENT: AXIAL RATIO AT 14, 14.25 AND 14.5 GHZ

3. EBBM Electromagnetic Design: Radiating Aperture

Once the individual RX and TX radiating elements have been defined, this section aims to group them in arrays and evaluate its performance. In particular, the ESA Building Block Module that is evaluated is formed by 8x8 radiating elements.

In order to strengthen the circular polarization and improve the axial ratio, the radiating elements are organized in 2x2 synchronous sub-arrays. A 90º physical sequential rotation is applied in each radiating element of every sub-array and, at the same time, a quadrature phase shifting correction is made. A synchronous 2x2 sub-array schematic is shown in the following figure. The specific phase shifts of the different port excitations needed to achieve RHCP and LCHP are also depicted.

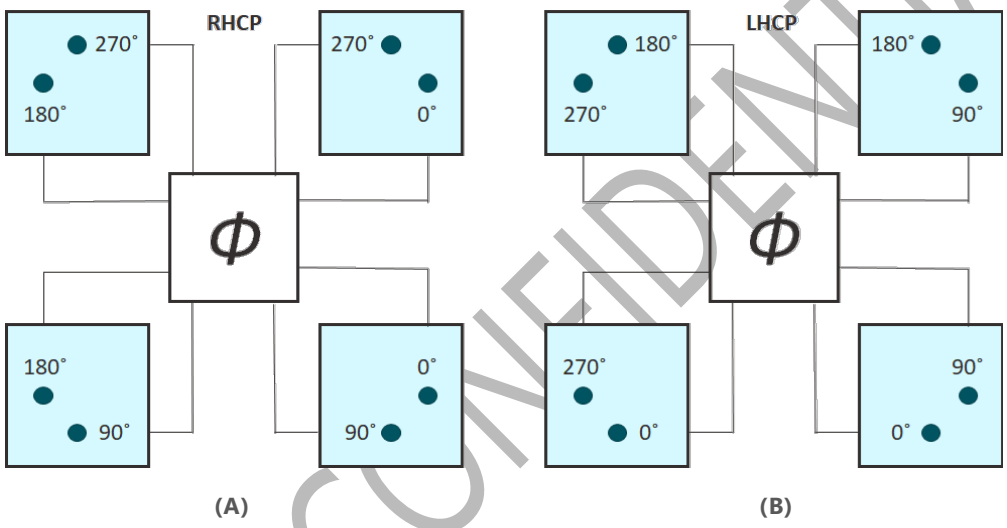

FIGURE 12: SEQUENTIAL ROTATION AND QUADRATURE PHASE SHIFTING FOR: (A) RHCP; (B) LHCP

Previous phase shift corrections need to be taken into account when performing beam steering. This is, they need to be added up with the pertinent phase excitations used to point to the desired direction.

The following figure shows the synchronous 2x2 sub-array configured in the radiofrequency simulation tool. Apart from improving the axial ratio, the sequential rotation simplifies the interconnection between patches and beamforming ICs. Each beamforming IC will be located at the the center of a 2x2 sub-array, at the bottom layer, managing the feeding of the four patches of the sub-array.

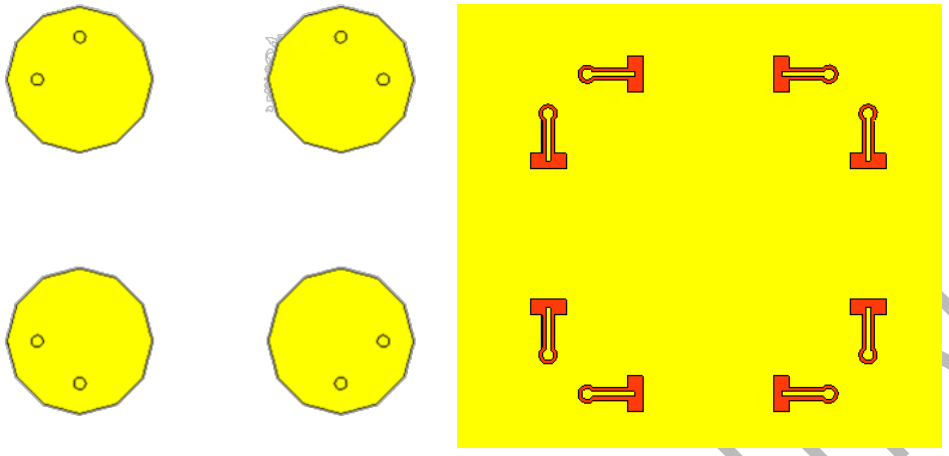

(A) (B)

FIGURE 13: 2X2 SUB-ARRAY AFTER SEQUENTIAL ROTATION APPLICATION: (A) RADIATING ELEMENTS LOCATED AT THE PCB TOP LAYER; (B) PORT CONFIGURATION AT THE PCB BOTTOM LAYER

As already mentioned, the EBBM radiating aperture will be formed by 8x8 radiating elements. This means that each EBBM radiating aperture will be formed by sixteen 2x2 synchronous sub-arrays. As an example, the following figure shows the RX EBBM radiating aperture. TX EBBM radiating module is similar, but with lower sizes and element separation.

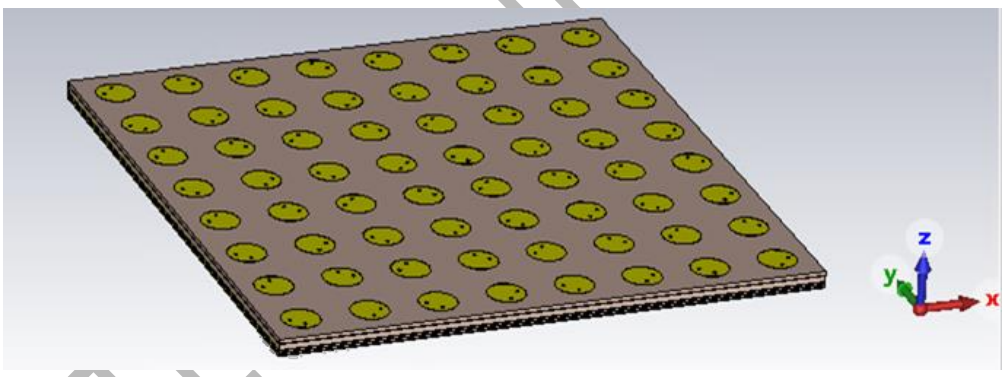

FIGURE 14: EBBM RADIATING APERTURE

CST Studio Suite is used to find the optimal separation between radiating elements in the previous structure. This process is made both for reception and transmission EBBM radiating apertures.

Element spacing is critical in a phased array performance and needs to be carefully tested. The array factor will be grating-lobe free from $\theta = 0^{\circ}$ to $\theta = \theta_0$, where θ is the off-axis angle (complementary angle of the elevation), as long as:

$$\frac{d}{\lambda} < \frac{1}{1+|\sin\theta_0|} \quad (1)$$

This is always true if $d = \frac{\lambda_{up}}{2}$, where λ_{up} is the wavelength associated to the upper limit of the working frequency band.

Regarding the phased array scanning performance, it is also beneficial to use the minimum possible separation between elements. When steering the beam to a specific elevation angle, the array coupled voltages tend to add in phase (leading to large reflections) when separation between elements gets increased.

However, the closer the radiating elements are, the bigger the coupling magnitude between elements is. Thus, there is a trade-off relation between grating-lobe free region, scanning behavior, and coupling magnitude, managed by the separation between elements.

The obtained solution and the radiofrequency simulation results are shown in the following sub-sections, for both the RX and TX EBBM radiating apertures.

3.1. RX EBBM Radiating Aperture

The separation solution found for the RX EBBM radiating aperture is the following:

- Separation between radiating elements:
  - 0.49λ@12.7GHz

Applying this solution, the RX EBMM radiating aperture gain obtained at boresight is between 21.2 and 22.2 dBi, for all the working frequency range. The highest gain value is obtained at the highest frequency, due to the larger electric size of the aperture at that frequency.

The following figure shows the radiation and total efficiency evolution when scanning, for all the working frequency range. Despite the efficiencies are shown when scanning from θ = 0º to θ = 60º (elevation from 90º to 30º), the maximum required scanning angle for the aperture is θ = 50º.

Both the radiation efficiency and the total efficiency behavior is similar when scanning between boresight and θ = 40º. However, both efficiencies decrease when reaching θ = 50º.

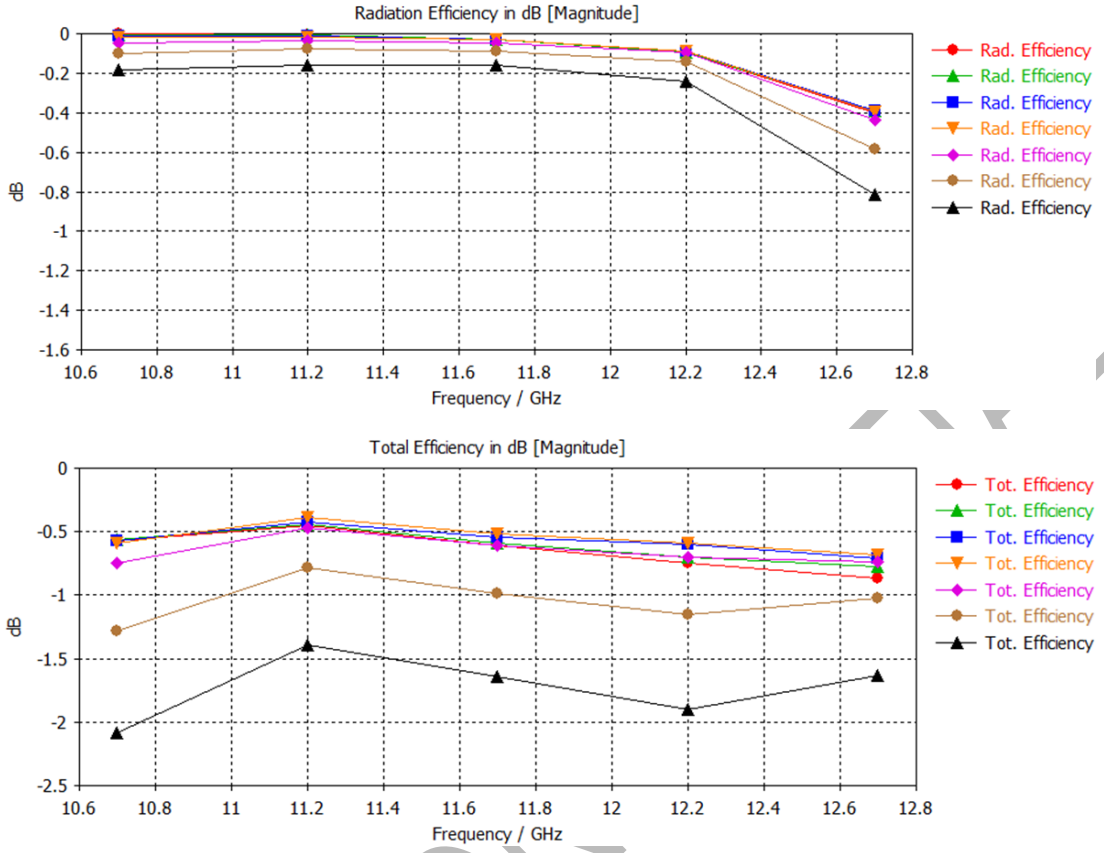

FIGURE 15: RX EBBM RADIATING APERTURE: EFFICIENCY WHEN SCANNING

The gain evolution when scanning at 11.2 GHz is shown in the following figure. The gain scanning behavior at other frequencies is very similar.

RX EBBM gain simulation results approximately follow a $\cos(\theta)^{1.3}$ gain drop variation when scanning from boresight to θ = 40º, for all frequencies. This gain variation is close to the ideal $\cos(\theta)$ variation (proportional to the projected aperture size towards the scanning direction). From θ = 40º to θ = 50º, the gain variation gets deteriorated, following the $\cos(\theta)^{1.5}$ expression.

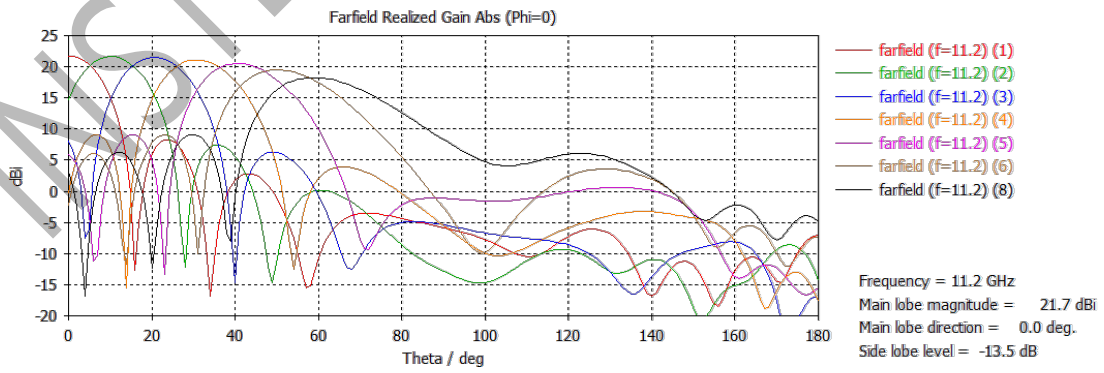

FIGURE 16: RX EBBM RADIATING APERTURE: GAIN BEHAVIOR WHEN SCANNING

Previous results also show that scan blindness, which is a typical phenomenon in phased array antennas, is not present in the operating scanning range.

Regarding the side lobe level (SLL), simulation results show that it is lower than -13 dB at boresight, for all frequencies. However, the SLL value drops to -10 dB at the scanning range limit θ = 50º. No tapering has been used. This can also be checked in the following figure, where the RX EBBM radiation patterns at boresight and θ = 50º are shown for the 11.2 GHz frequency.

The following figure also shows that, when pointing to boresight, the radiation pattern is perfectly centered. The pointing error observed in the individual radiating element simulations does not exist in the array configuration due to the sequential rotation configuration.

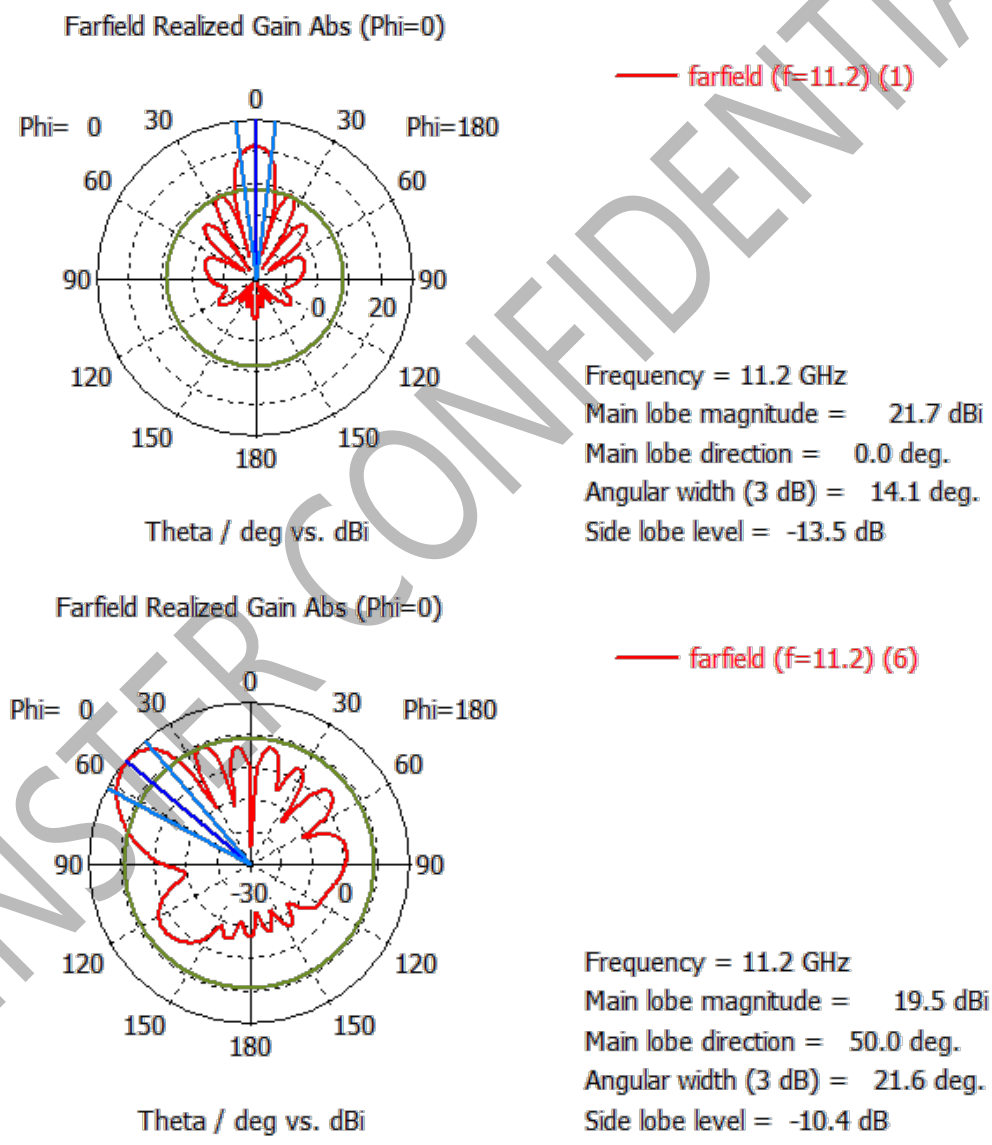

FIGURE 17: RX EBBM RADIATING APERTURE RADIATION PATTERN (GAIN)

Following figures show the axial ratio results for the lower, central, and upper RX working frequencies, respectively. For each frequency, four different graphs corresponding to different off-axis pointing angles are presented: θ = 0º, θ = 30º, θ = 40º, and θ = 50º.

As expected, there is an improvement in the axial ratio compared with the values obtained in the individual radiating element. In fact, the axial ratio is below 0.1 dB at boresight (θ = 0º) for all working frequencies. The worst axial ratio result, 3.3 dB, has been obtained at the upper RX working frequency and the highest scanning angle: 12.7 GHz and θ = 50º (40º elevation). This value is expected to improve when increasing the radiating aperture size and directivity.

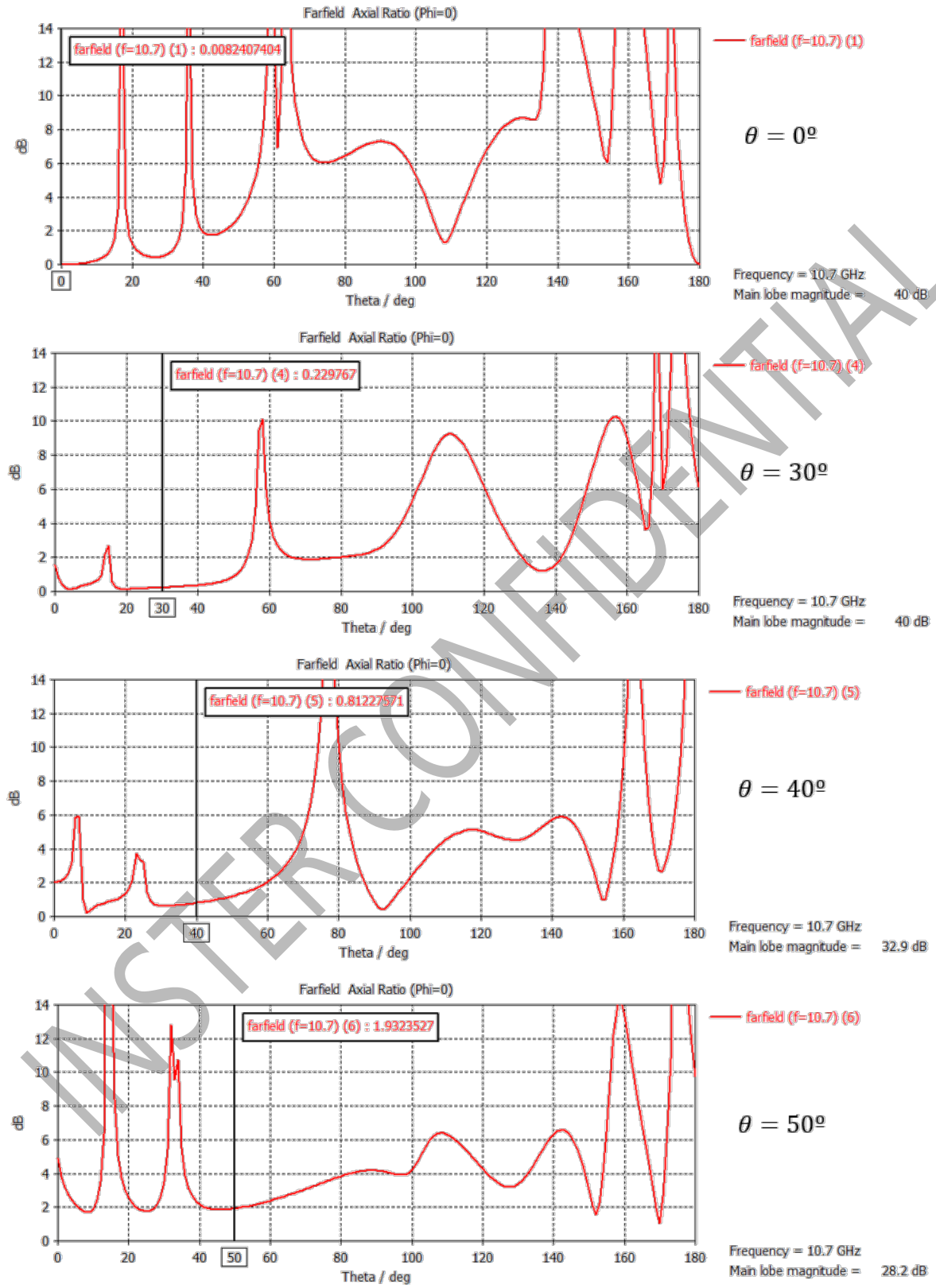

FIGURE 18: RX EBBM RADIATING APERTURE AXIAL RATIO AT 10.7 GHZ

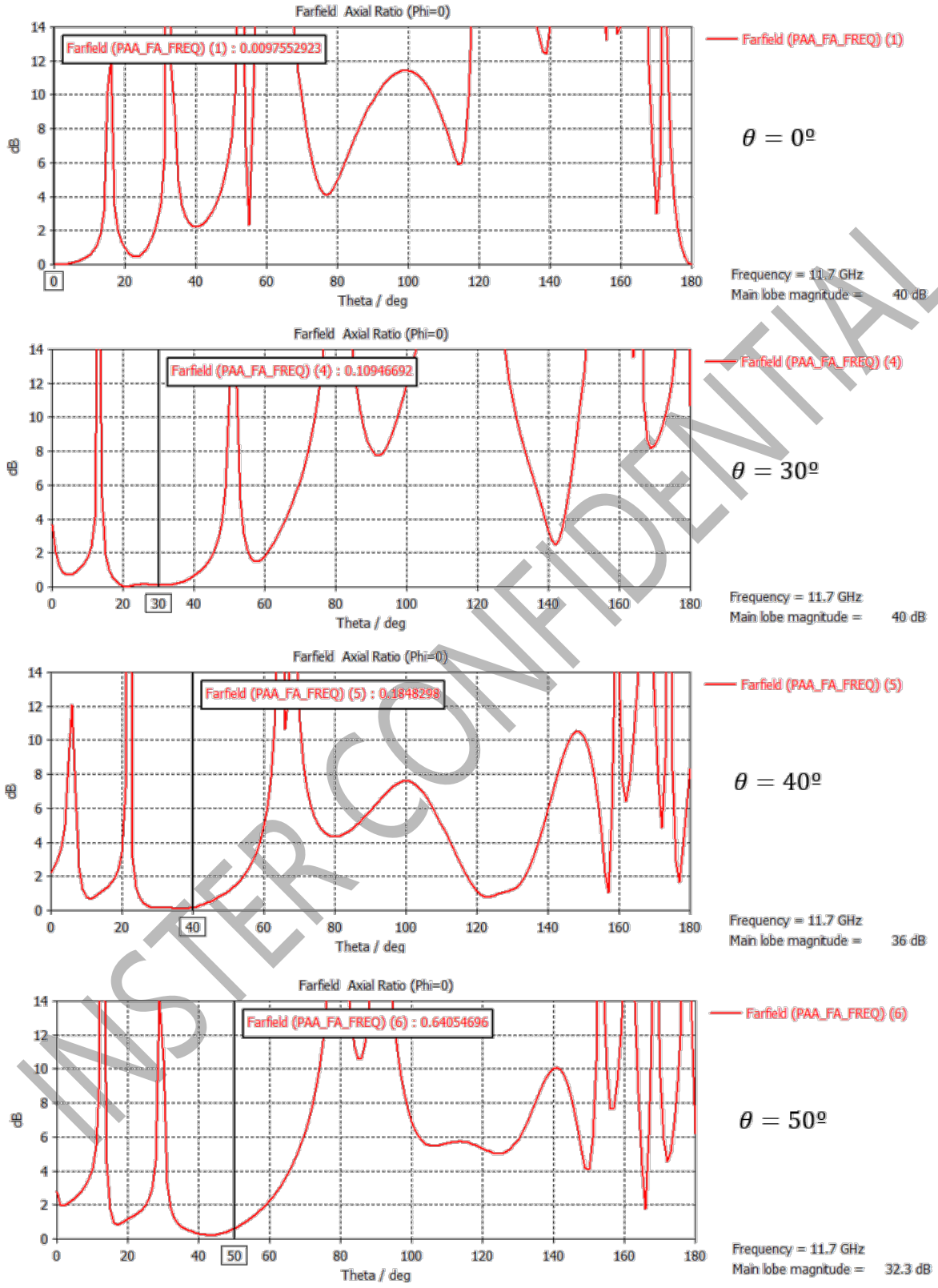

FIGURE 19: RX EBBM RADIATING APERTURE AXIAL RATIO AT 11.7 GHZ

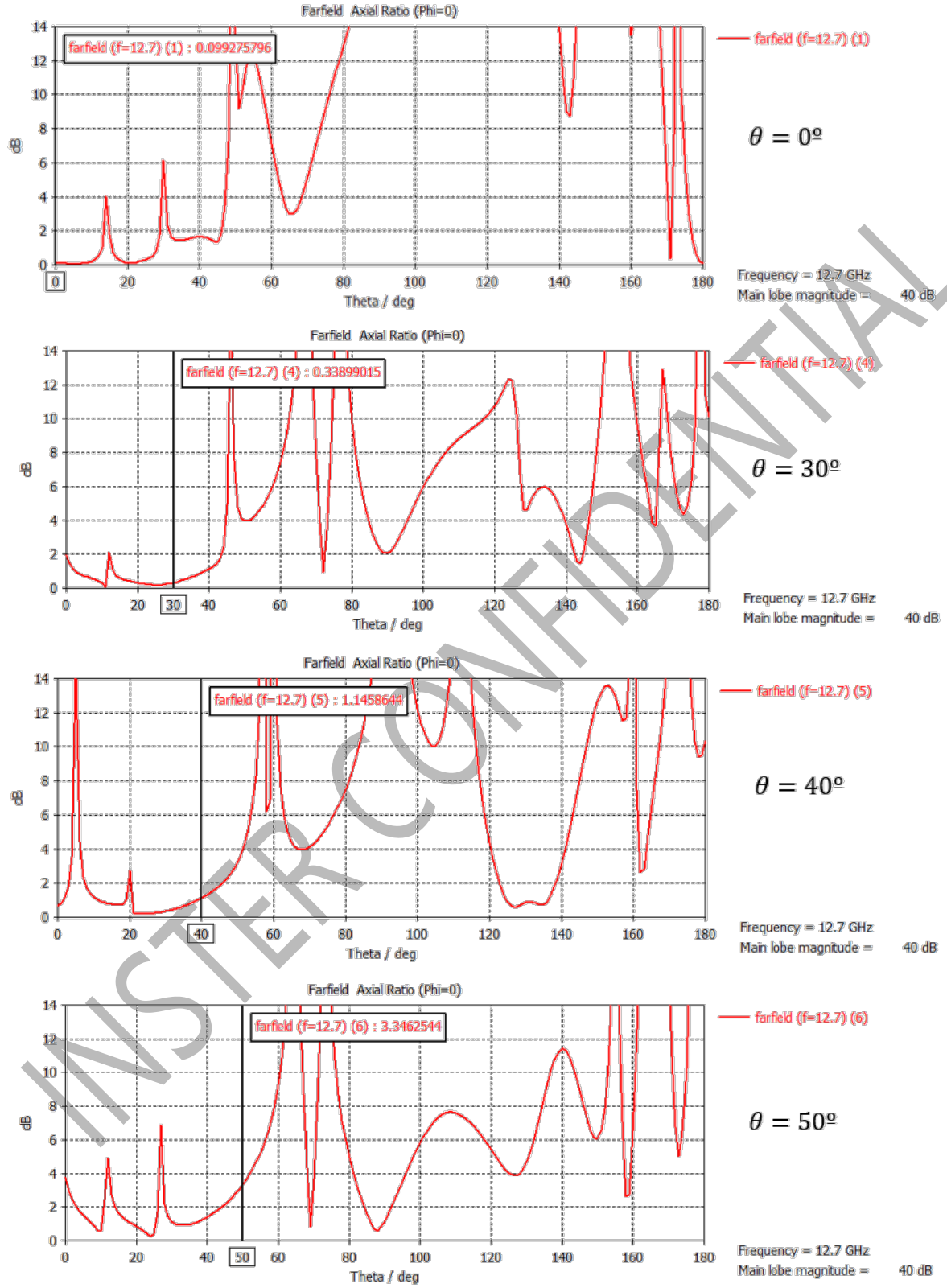

FIGURE 20: RX EBBM RADIATING APERTURE AXIAL RATIO AT 12.7 GHZ (WORST CASE)

3.2. TX EBBM Radiating Aperture

The separation solution found for the TX EBBM radiating aperture is the following:

- Separation between radiating elements of the same 2x2 sub-array:
  - 0.50λ@12.7GHz
- Separation between radiating elements of neighboring 2x2 sub-arrays:
  - 0.55λ@12.7GHz

Following this solution, the TX EBBM radiating aperture gain at boresight is between 22.1 and 23.0 dBi, for the whole working frequency range. Again, the highest gain is obtained at the highest working frequency.

The radiation and total efficiencies obtained when scanning, for all the frequencies, are shown in the following figure. A smooth degradation in both the radiation and the total efficiency can be observed when scanning up to θ = 50º.

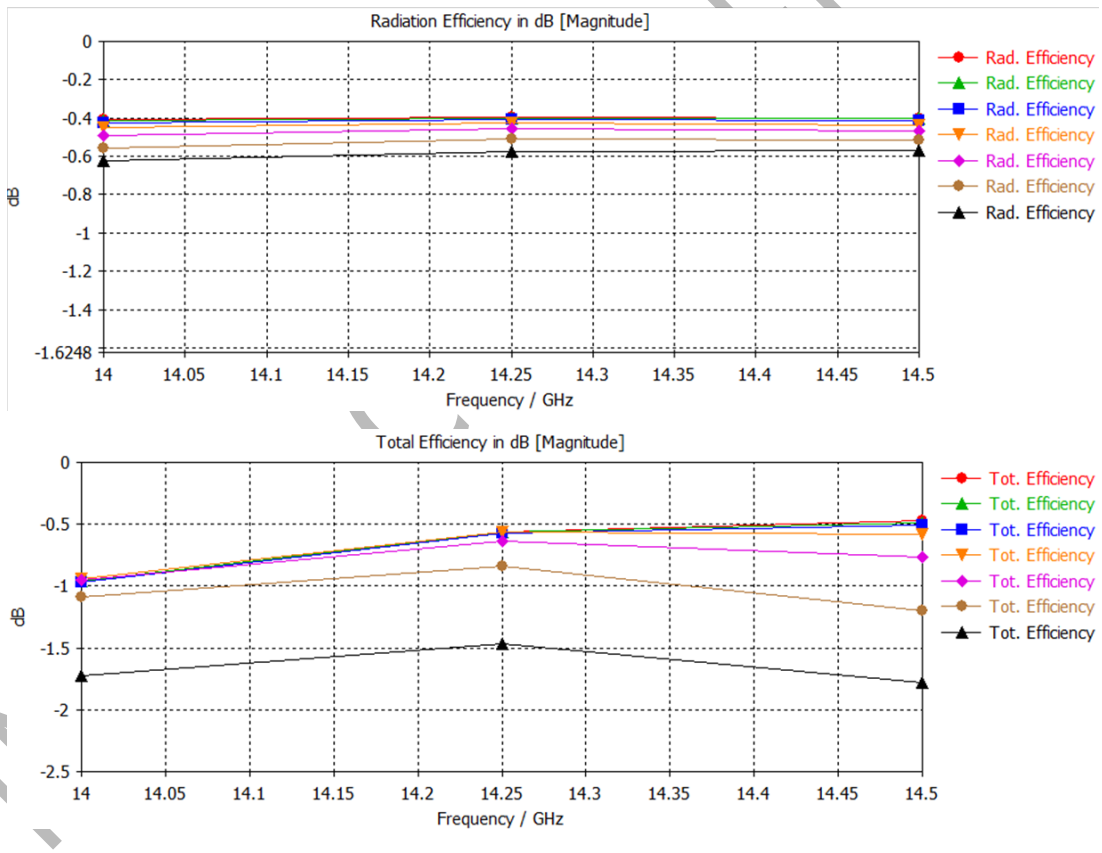

FIGURE 21: TX EBBM RADIATING APERTURE: EFFICIENCY WHEN SCANNING

The next figure shows the gain behavior when scanning at 14 GHz. This behavior is similar at other evaluated frequencies.

In this case, the TX EBBM gain simulation results follow a $\cos(\theta)^{1.2}$ variation from boresight to θ = 40º, for all frequencies. Between θ = 40º and θ = 50º, the gain approximately follows a $\cos(\theta)^{1.5}$ variation. Again, the scan blindness phenomenon is not present in the operating scanning range.

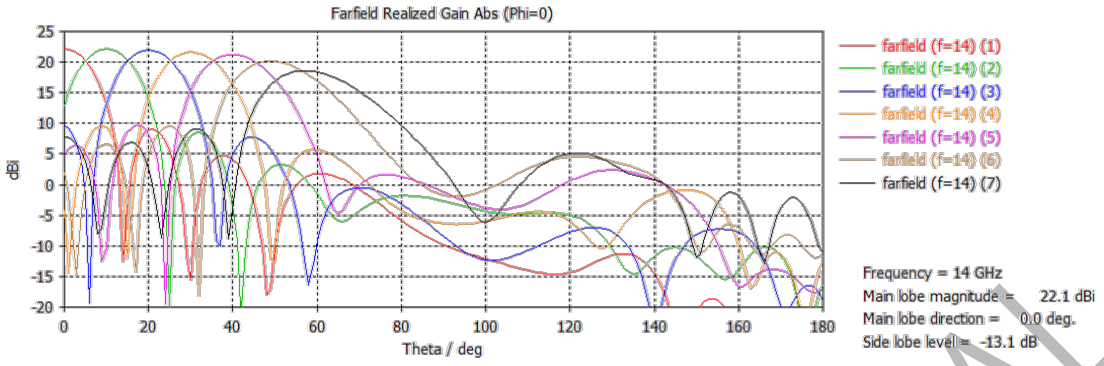

FIGURE 22: TX EBBM RADIATING APERTURE: GAIN BEHAVIOR WHEN SCANNING

The SLL obtained in simulation, for all frequencies, is below -13 dB at boresight. In the worst case, it drops to -9.2 dB at the scanning range boundary θ = 50º. No tapering has been used.

The TX EBBM radiation patterns at boresight and θ = 50º, for the 14 GHz frequency, are shown in the following figure. Again, the pointing error observed in the individual radiating element simulations are not present in the EBBM configuration when pointing to boresight, due to the sequential rotation configuration.

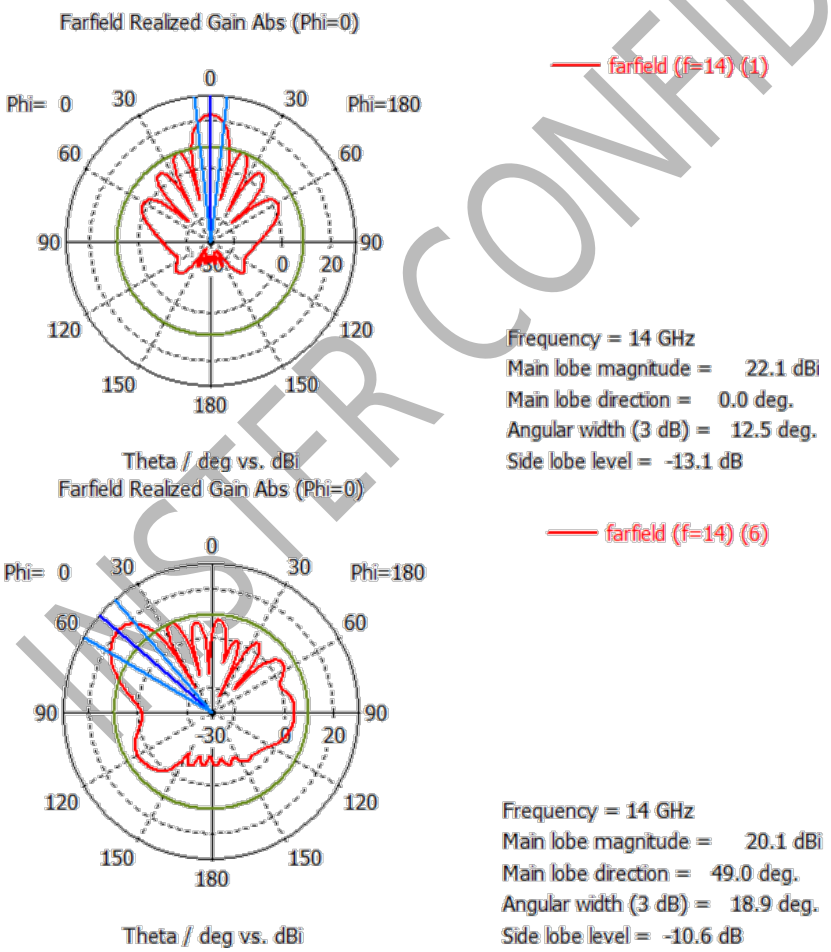

FIGURE 23: TX EBBM RADIATING APERTURE RADIATION PATTERN (GAIN)

Finally, the TX EBBM axial ratio results for the lower, central, and upper TX working frequencies are shown in the following figures. For each frequency, four different graphs corresponding to θ = 0º, θ = 30º, θ = 40º, and θ = 50º off-axis pointing angles are presented. The axial ratio value obtained through simulation is below 0.1 dB at boresight (θ = 0º), for all frequencies. This value gets deteriorated when scanning, achieving 3.6 dB at the highest TX working frequency and the maximum scanning angle θ = 50º (40º elevation). This value is expected to improve in the whole antenna due to the increase of the directivity.

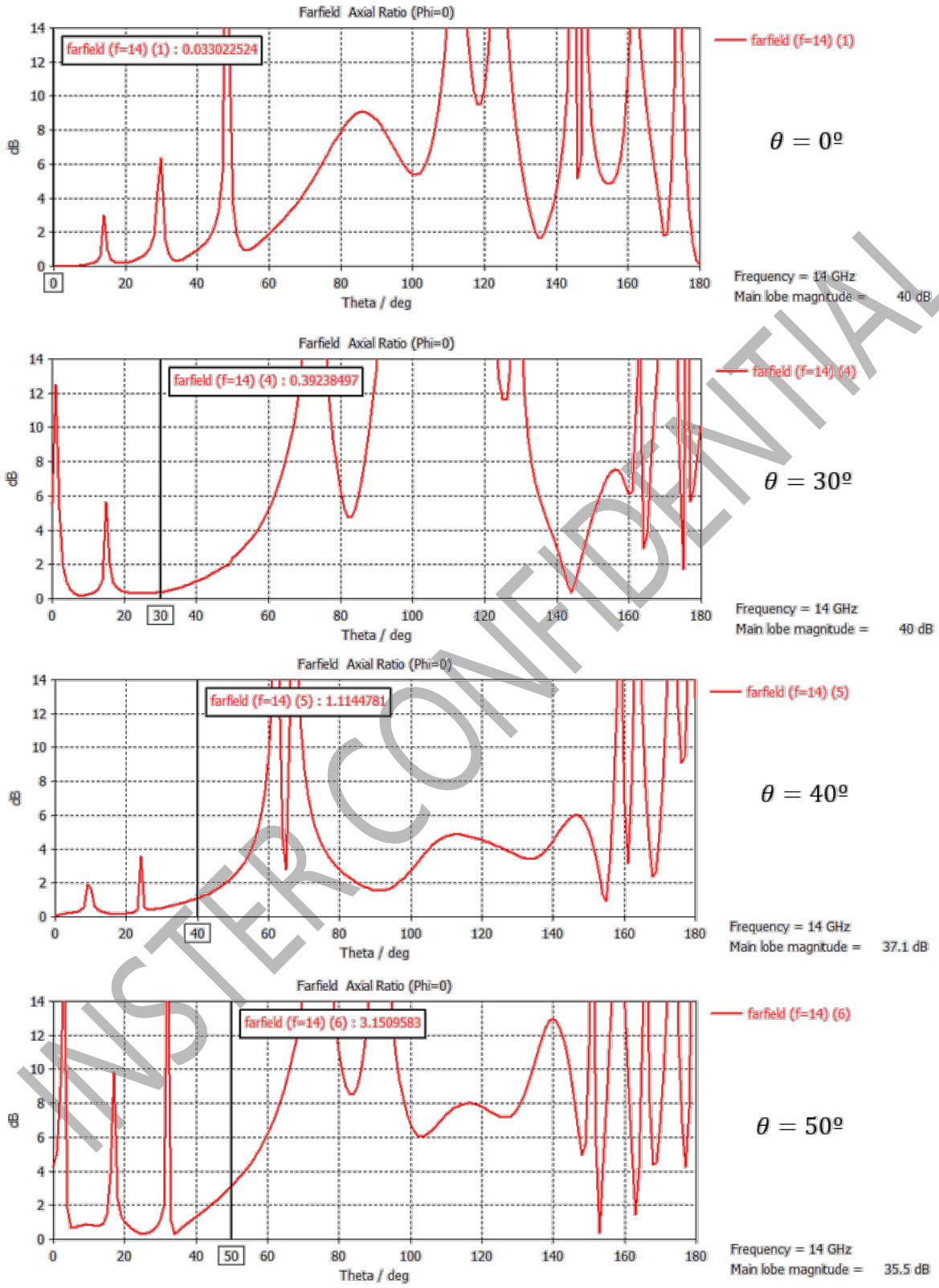

FIGURE 24: TX EBBM RADIATING APERTURE AXIAL RATIO AT 14 GHZ

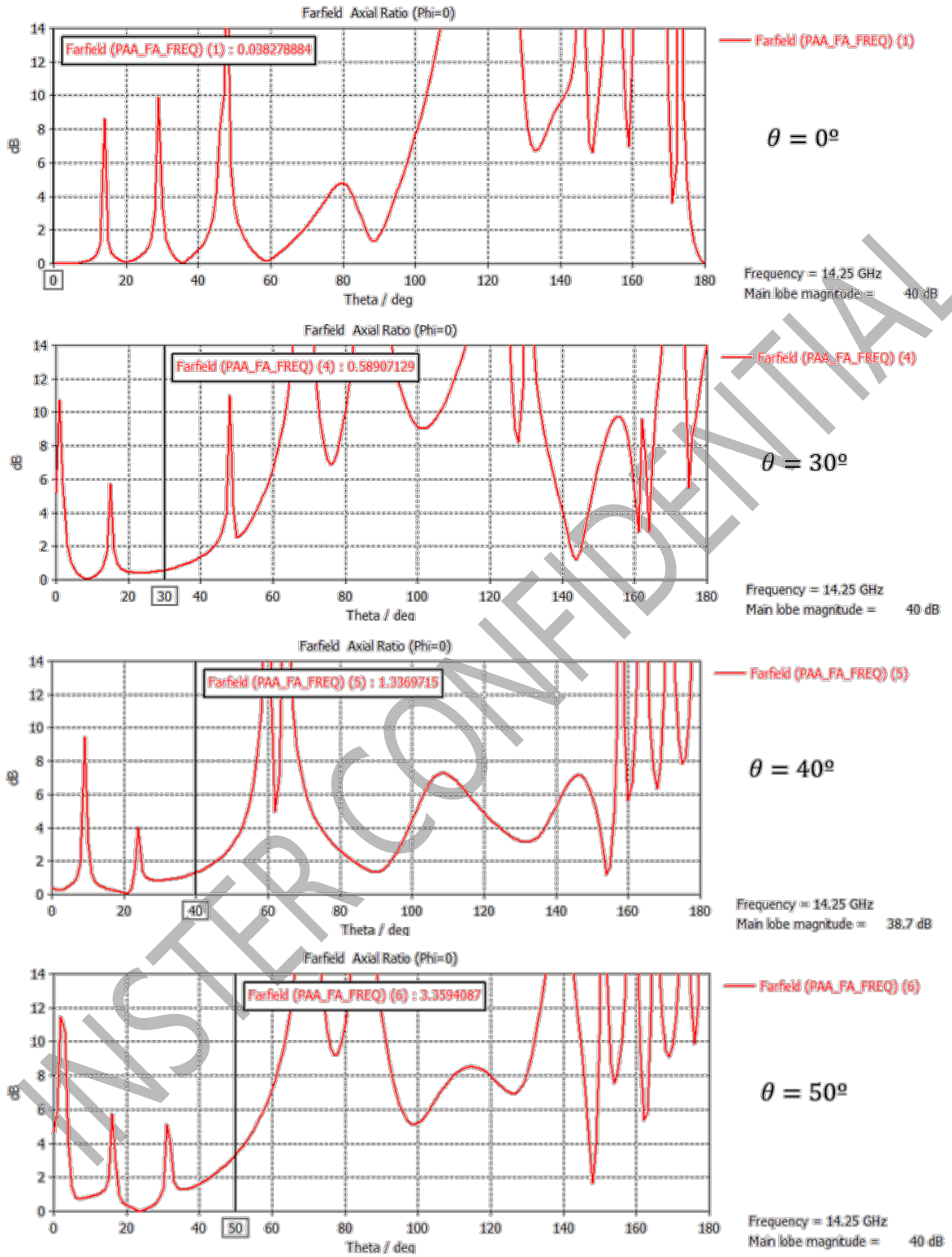

FIGURE 25: TX EBBM RADIATING APERTURE AXIAL RATIO AT 14.25 GHZ

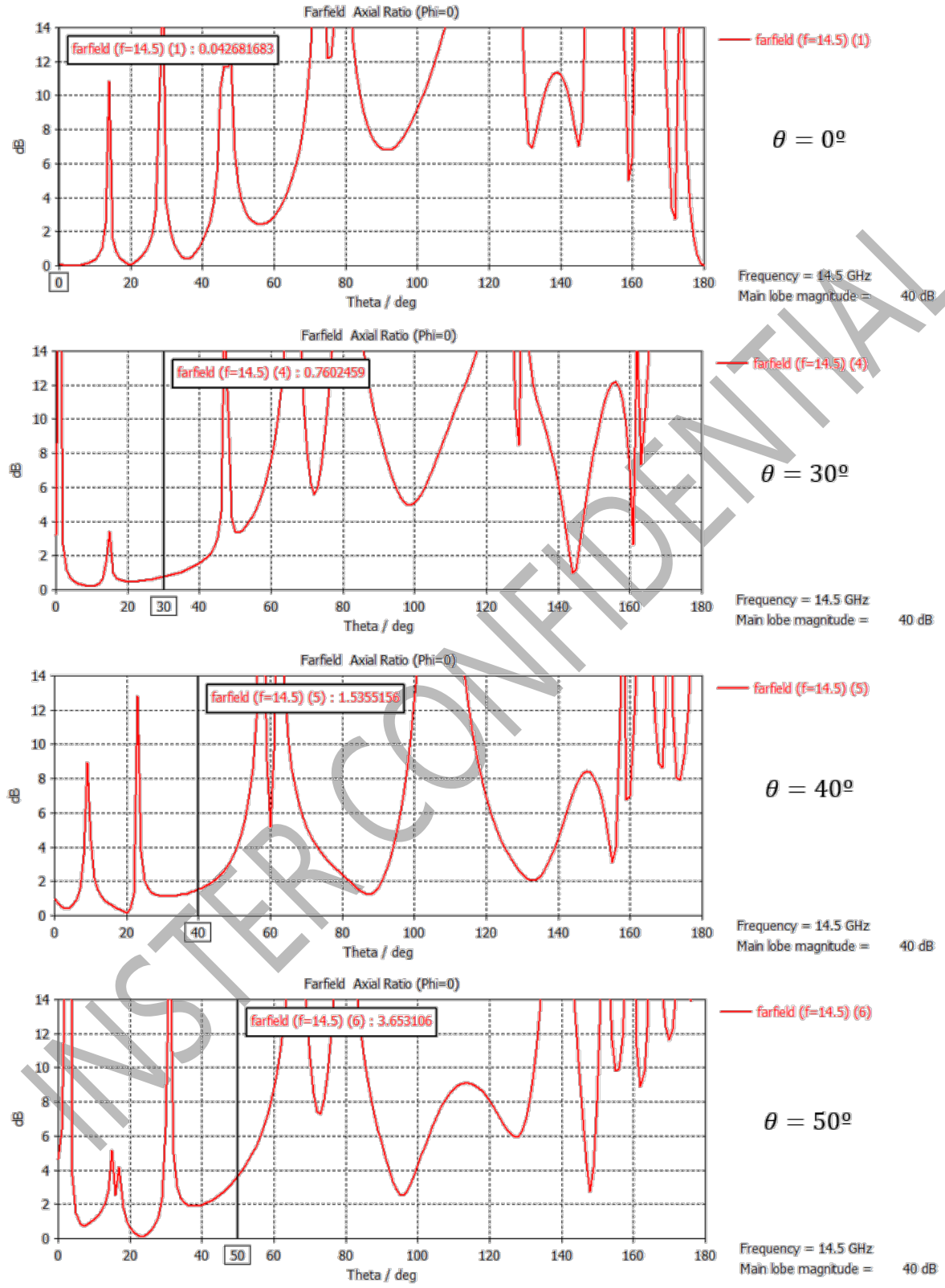

FIGURE 26: TX EBBM RADIATING APERTURE AXIAL RATIO AT 14.5 GHZ (WORST CASE)

4. EBBM Electromagnetic Design: RF Feeding Network

The EBBM radiating aperture simulation shown in previous chapter does not include the beamforming ICs and the RF feeding network. The pre-design of the feeding network is presented in this chapter.

A different feeding network is needed for the RX and the TX EBBM radiating apertures. The RX feeding network is in charge of the combination of the RX beamforming ICs outputs forming the RX RF common output, while the TX feeding network is responsible of splitting the TX RF common input in order to feed all the TX beamforming ICs.

Both feeding networks are designed to follow a symmetrical distribution. In the next sections both feeding network designs are explained, and simulation results are shown. The starting point is the single combiner and splitter designs. Both the combiner and the splitter designs follow a two-port Wilkinson power combiner/splitter topology [14], [15]:

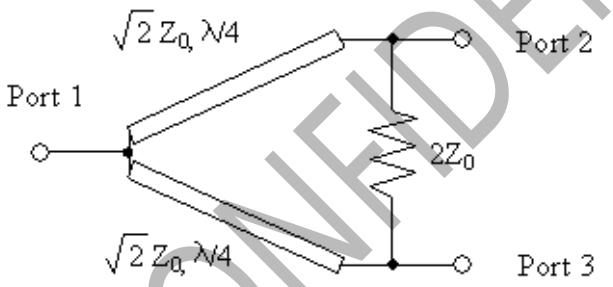

FIGURE 27: TWO-PORT WILKINSON SPLITTER/COMBINER

In the next figure a scheme of the EBBM bottom layer is depicted. The scheme is applicable both in reception and transmission. The RF signal distribution is shown, where combiners/splitter are represented in yellow.

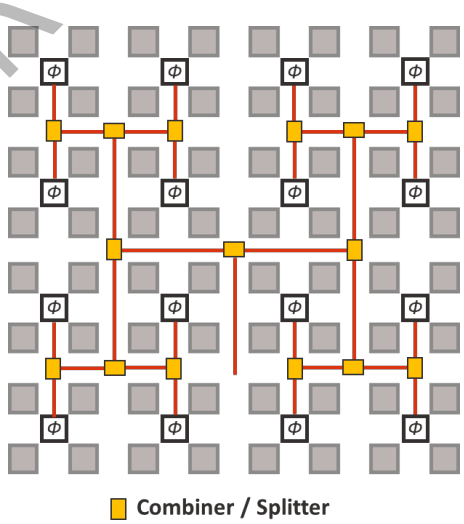

FIGURE 28: EBBM FEEDING NETWORK SCHEME

Four stages of signal combination/splitting are needed to reach every beamforming IC. A total of 15 combiners/splitters are needed for creating the EBBM RF reception/transmission feeding network.

4.1. Combiner design and simulation results

The combiner is designed targeting a good isolation between inputs, a low input return, and high performance in terms of the transmission coefficient between the inputs and the output. As already mentioned, the design corresponds to a two-port Wilkinson power combiner topology.

According to the PCB stack-up shown in Figure 2, and considering that the feeding network should be placed in bottom layer L9, the combiner is designed following the rules summarized in the table below:

PARAMETER	VALUE
Frequency range	10.7 – 12.7 GHz
Dielectric material	Prepreg, ε_r 2.94, tanδ 0.003
Substrate height	5 mils
Copper height	1.45 mils

TABLE 5: DESIGN RULES FOR THE COMBINER

Figure 29 shows the schematic defined in QucsStudio for the design and simulation of the combiner. Combiner input ports are considered as ports 2 and 3, while port 1 is the output port. According to the chosen topology, a 100 Ω resistor is used to improve the isolation between ports 2 and 3. The schematic has been configured according to the optimal form factor to be placed between beamforming ICs. The layout associated with said configuration is depicted in Figure 30.

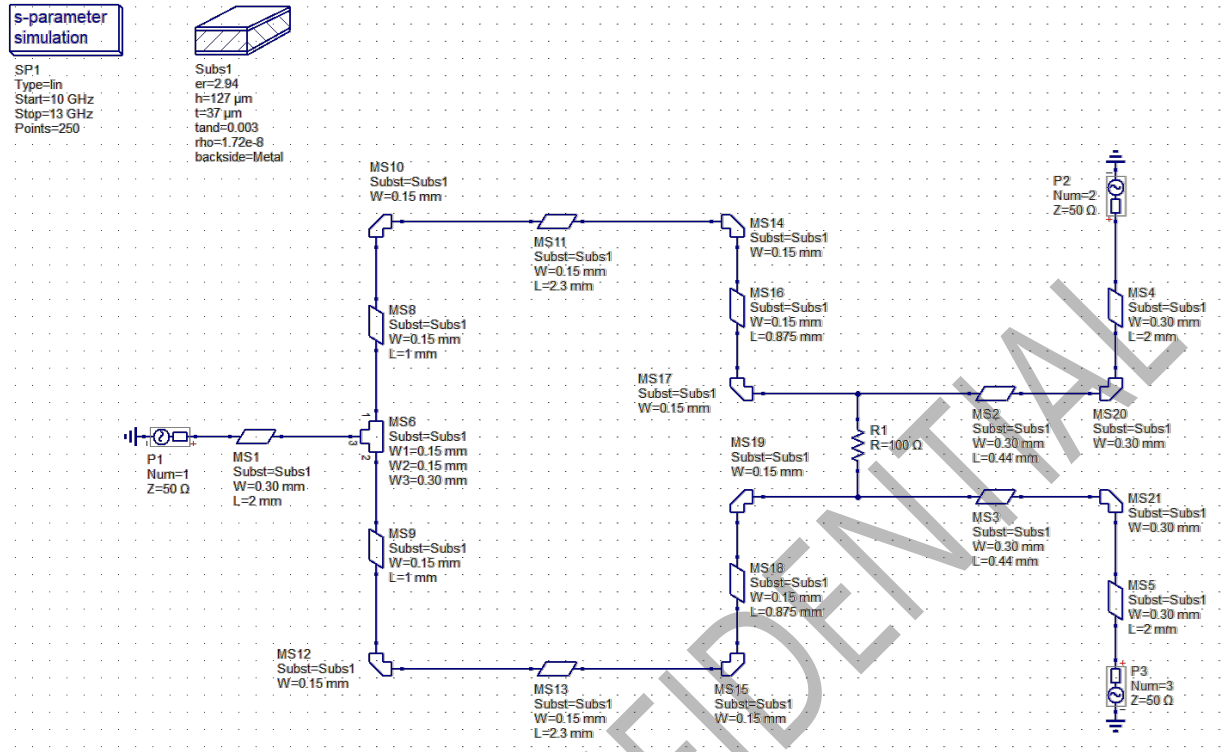

FIGURE 29: COMBINER SCHEMATIC DESIGN

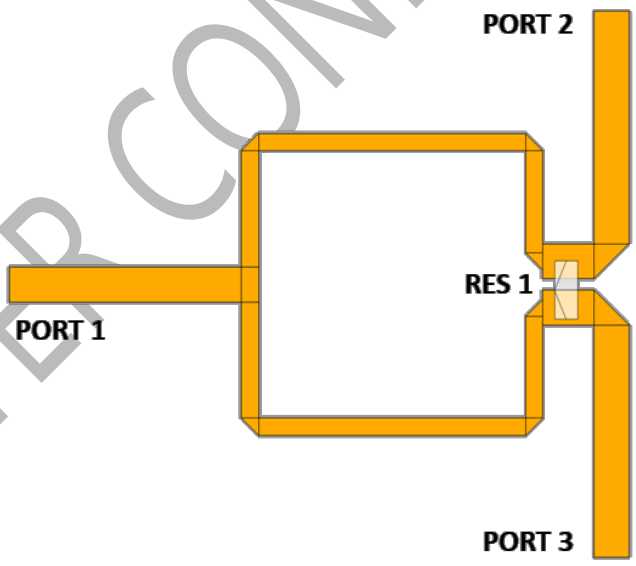

FIGURE 30: COMBINER LAYOUT DESIGN

The following figure shows the simulated S-Parameters of the combiner. Port numeration from previous figures is followed. According to the simulation results (summarized in Table 6) the combiner is matched on all ports, the input ports are highly isolated, and the transmission coefficient is, as expected, close to -3.0 dB across the entire operating frequency range. It should be noted that

there are some losses in the microstrip lines and mitered bends, and that is why the $S_{2,1}$ parameter is not exactly at the theoretical -3.0 dB level.

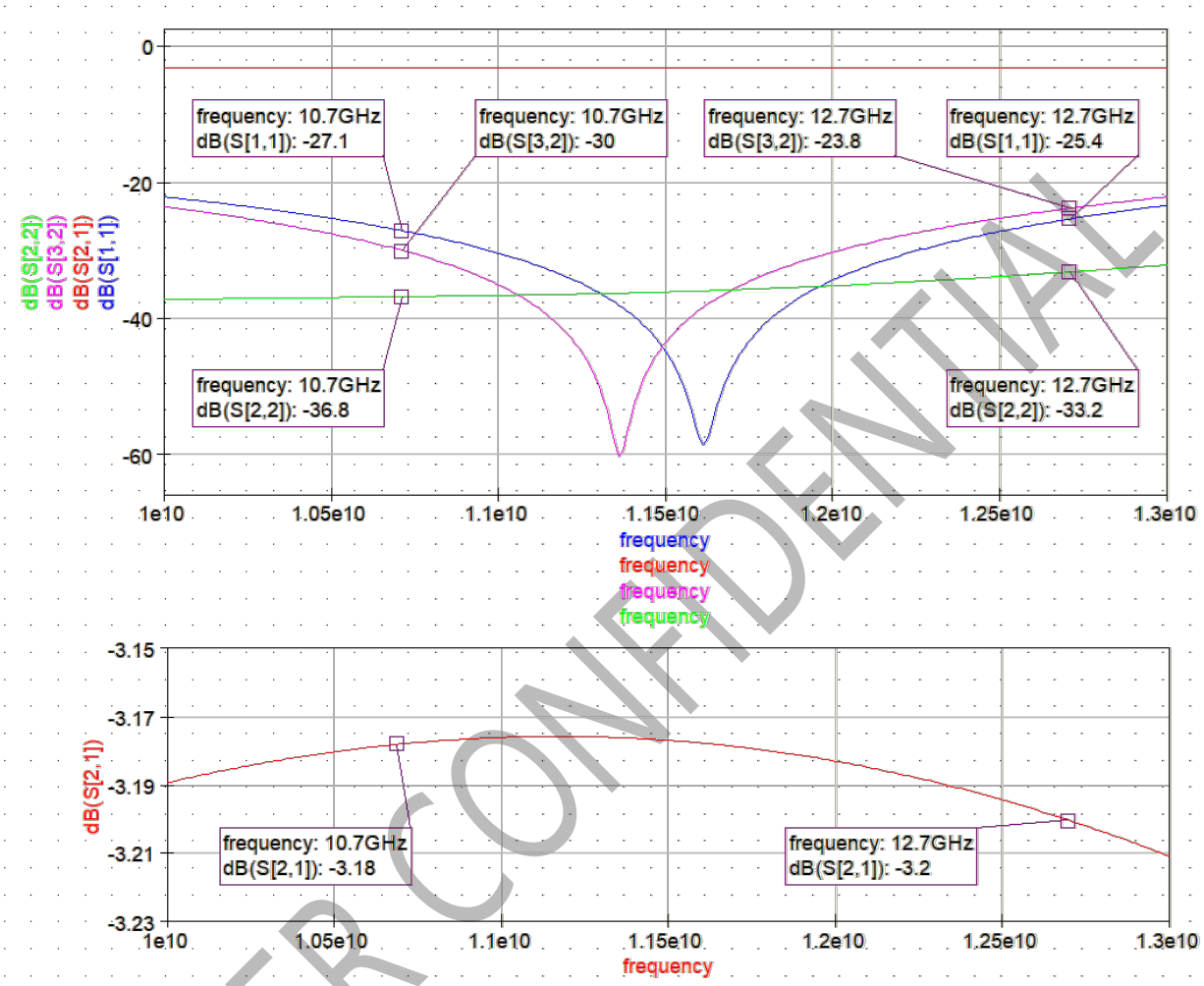

FIGURE 31: COMBINER SIMULATED S-PARAMETERS

PARAMETER	VALUE
Frequency range	14.0 – 14.5 GHz
Reflection coefficient of input ports	< -33.2 dB
Transmission coefficient	> -3.2 dB
Isolation between input ports	< -23.8 dB
Reflection coefficient of output port	< -25.4 dB

TABLE 6: COMBINER SIMULATED PERFORMANCE

4.2. RX EBBM feeding network

As previously explained, the RX EBBM feeding network is created by using four stages of combiners. The resulting layout of the RX EBBM feeding network is shown in the following figure. Port 1 is the common RF output, while the other sixteen ports would be connected to the RF output of each beamforming IC. Figure 33 shows the S-parameters obtained in simulation, which are in turn summarized in Table 7.

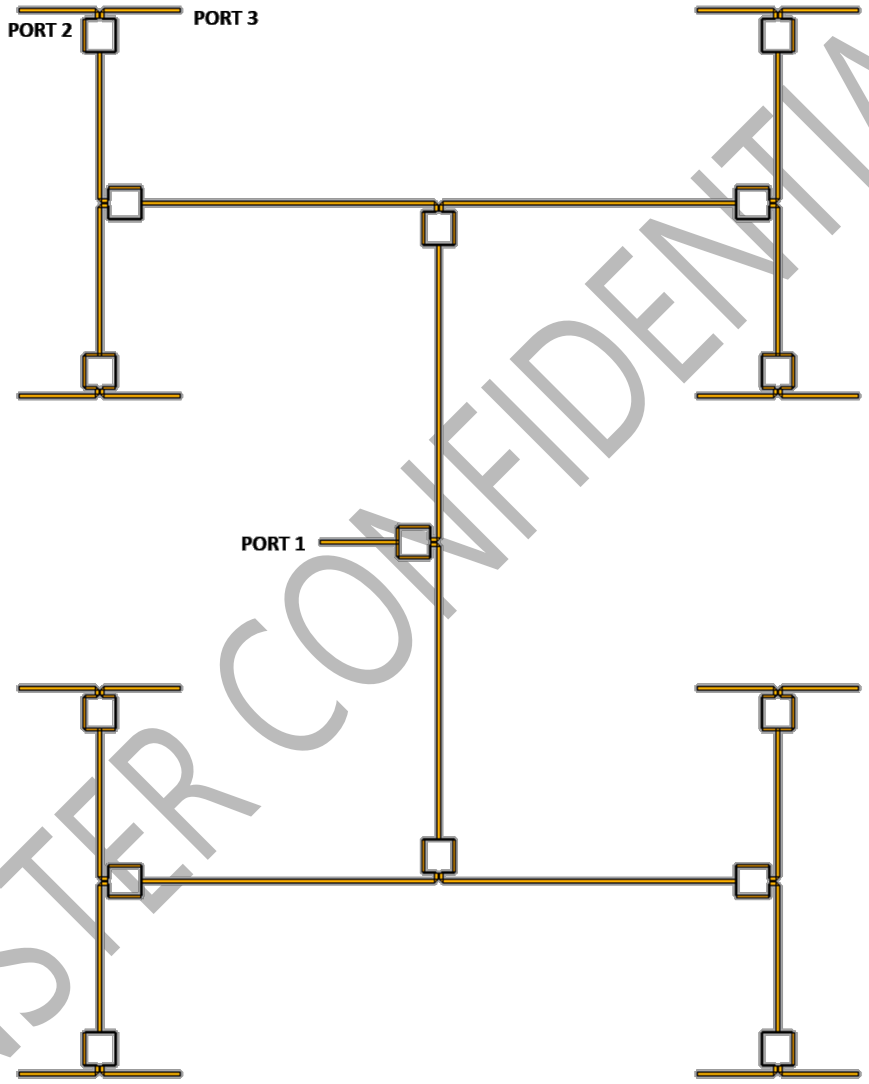

FIGURE 32: LAYOUT OF THE RX EBBM FEEDING NETWORK

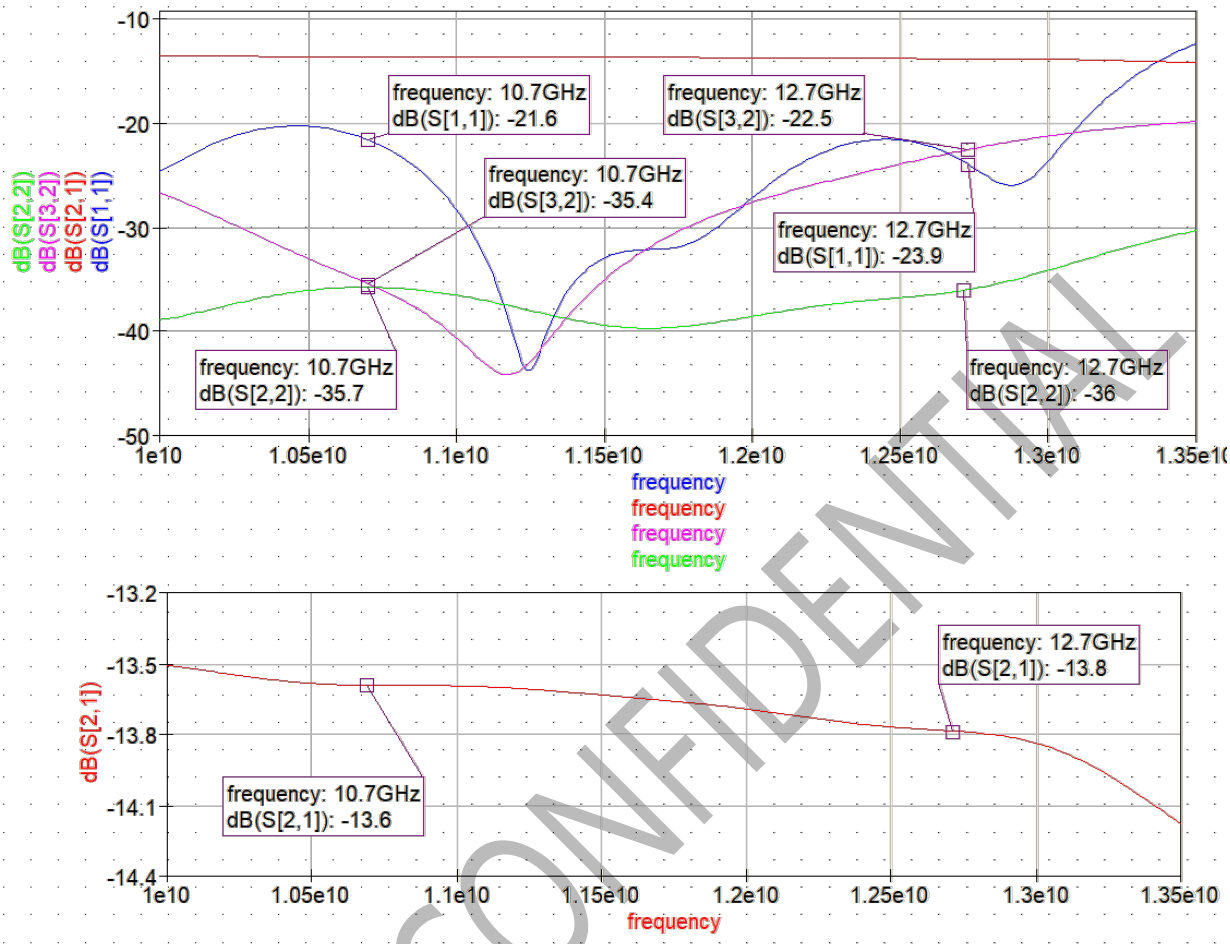

FIGURE 33: SIMULATED S-PARAMETERS OF THE RX EBBM FEEDING NETWORK

PARAMETER	VALUE
Frequency range	10.7 – 12.7 GHz
Reflection coefficient of input ports	< -21.6 dB
Transmission coefficient to common RF port (port 1) using only 1 input	> -13.8 dB

TABLE 7: SIMULATED PERFORMANCE OF THE RX EBBM FEEDING NETWORK

4.3. Splitter design and simulation results

The splitter is designed targeting a low input return, a good isolation between output ports, and high performance in terms of the transmission coefficient between the input and the outputs. The splitter topology is based on a two-port Wilkinson divider.

Next table summarizes the rules followed in the splitter design:

PARAMETER	VALUE
Frequency range	14.0 – 14.5 GHz
Dielectric material	Prepreg, ε_r 2.94, tanδ 0.003
Substrate height	5 mils
Copper height	1.45 mils

TABLE 8: DESIGN RULES FOR THE SPLITTER

Following figures show, respectively, the schematic defined for the splitter design and its associated layout in QucsStudio. Port 1 is the input port, while ports 2 and 3 are the output ports. According to the chosen topology, a 100 Ω resistor is used to improve the isolation between ports 2 and 3.

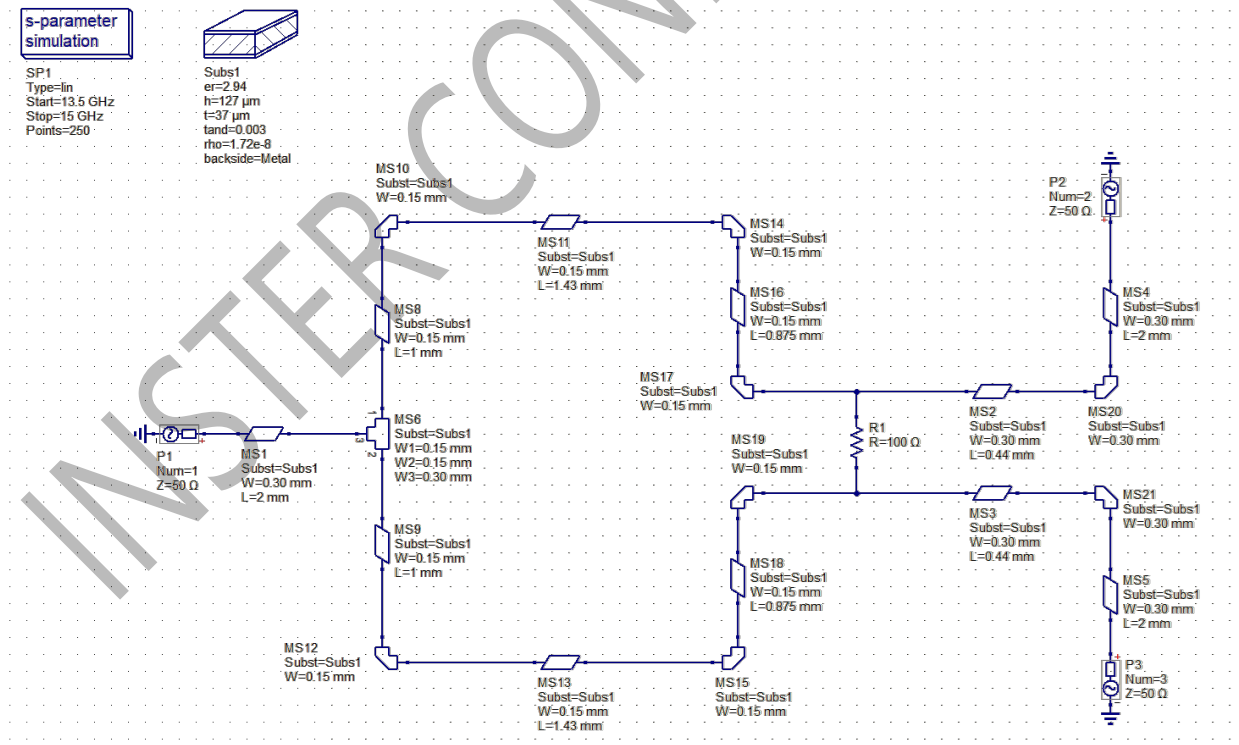

FIGURE 34: SPLITTER SCHEMATIC DESIGN

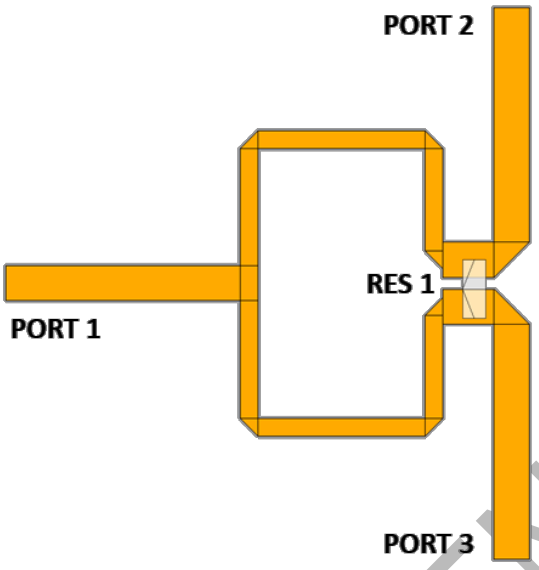

FIGURE 35: SPLITTER LAYOUT DESIGN

The simulated S-Parameters of the previous design are depicted in Figure 36 and summarized in Table 9. These simulation results show a good matching in both the input and the output ports, a great isolation between the output ports, and the transmission coefficient is close to the theoretical -3.0 dB across the whole operating frequency range.

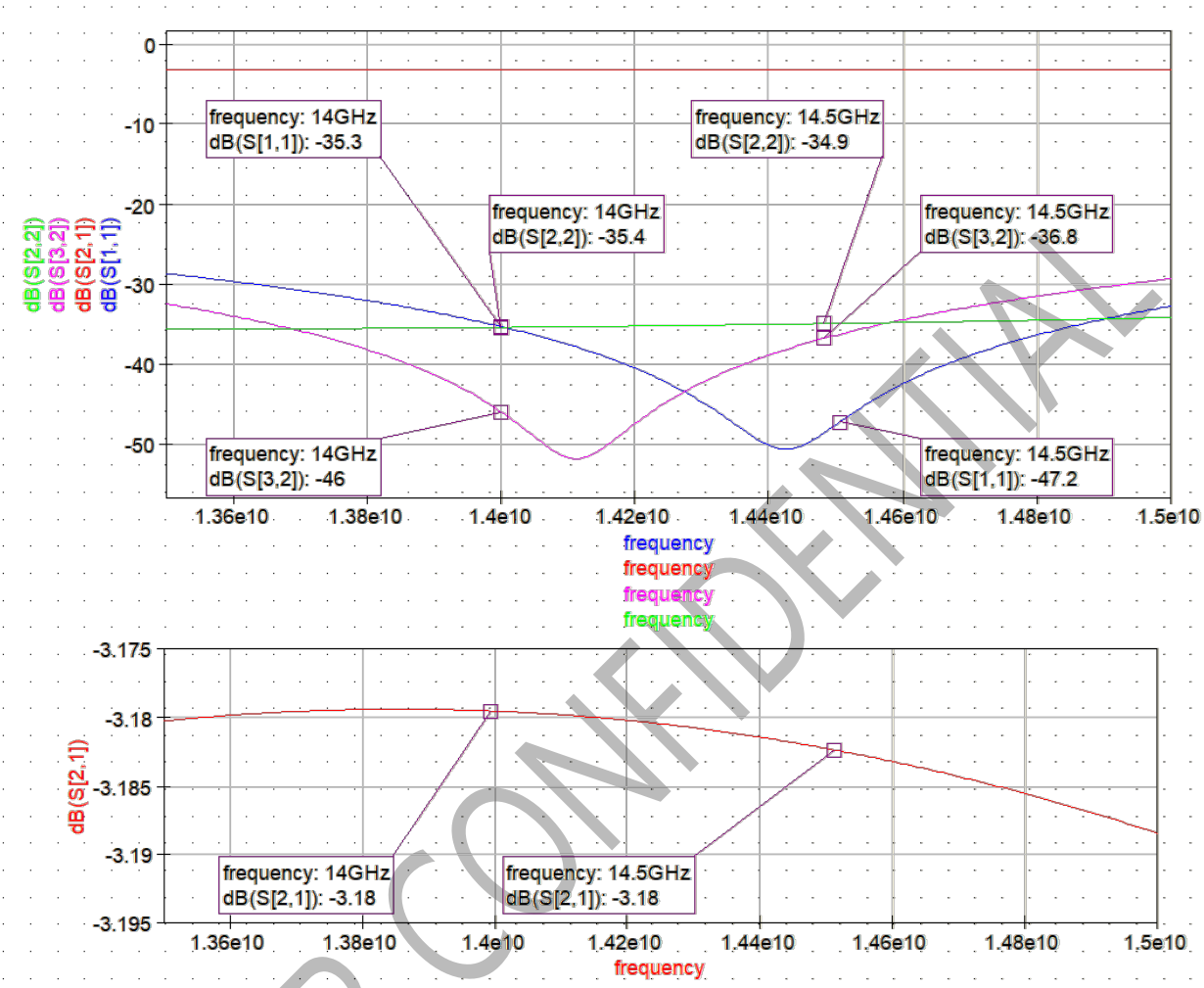

FIGURE 36: SPLITTER SIMULATED S-PARAMETERS

PARAMETER	VALUE
Frequency range	14.0 – 14.5 GHz
Reflection coefficient of input port	< -35.3 dB
Transmission coefficient	> -3.2 dB
Isolation between output ports	< -36.8 dB
Reflection coefficient of output ports	< -34.9 dB

TABLE 9: SPLITTER SIMULATED PERFORMANCE

4.4. TX EBBM feeding network

Four stages of dividers are used to create the TX EBBM feeding network, which is depicted in the following figure. Port 1 is the RF input port of the network, while the rest of the ports are the RF inputs of the beamforming ICs. Figure 38 shows the S-parameters obtained by means of EM simulations. The TX EBBM feeding network performance is summarized in Table 10.

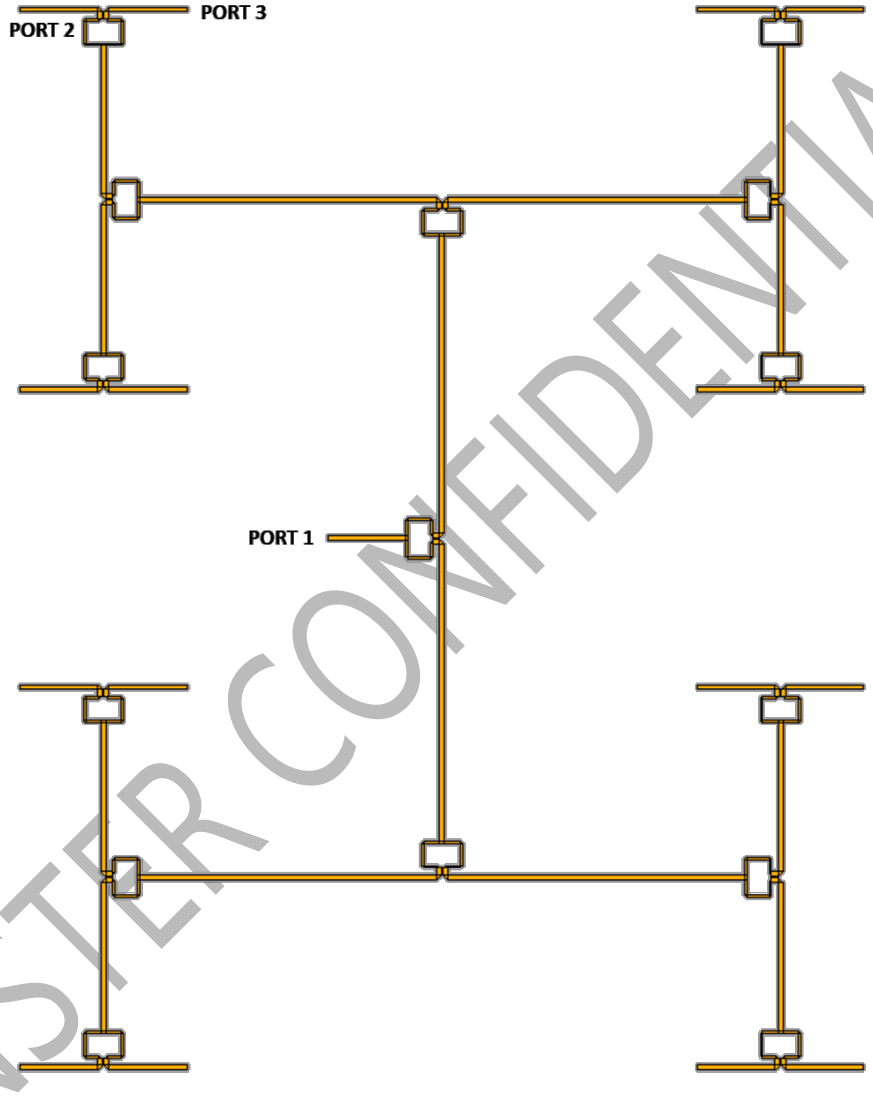

FIGURE 37: LAYOUT OF THE TX EBBM FEEDING NETWORK

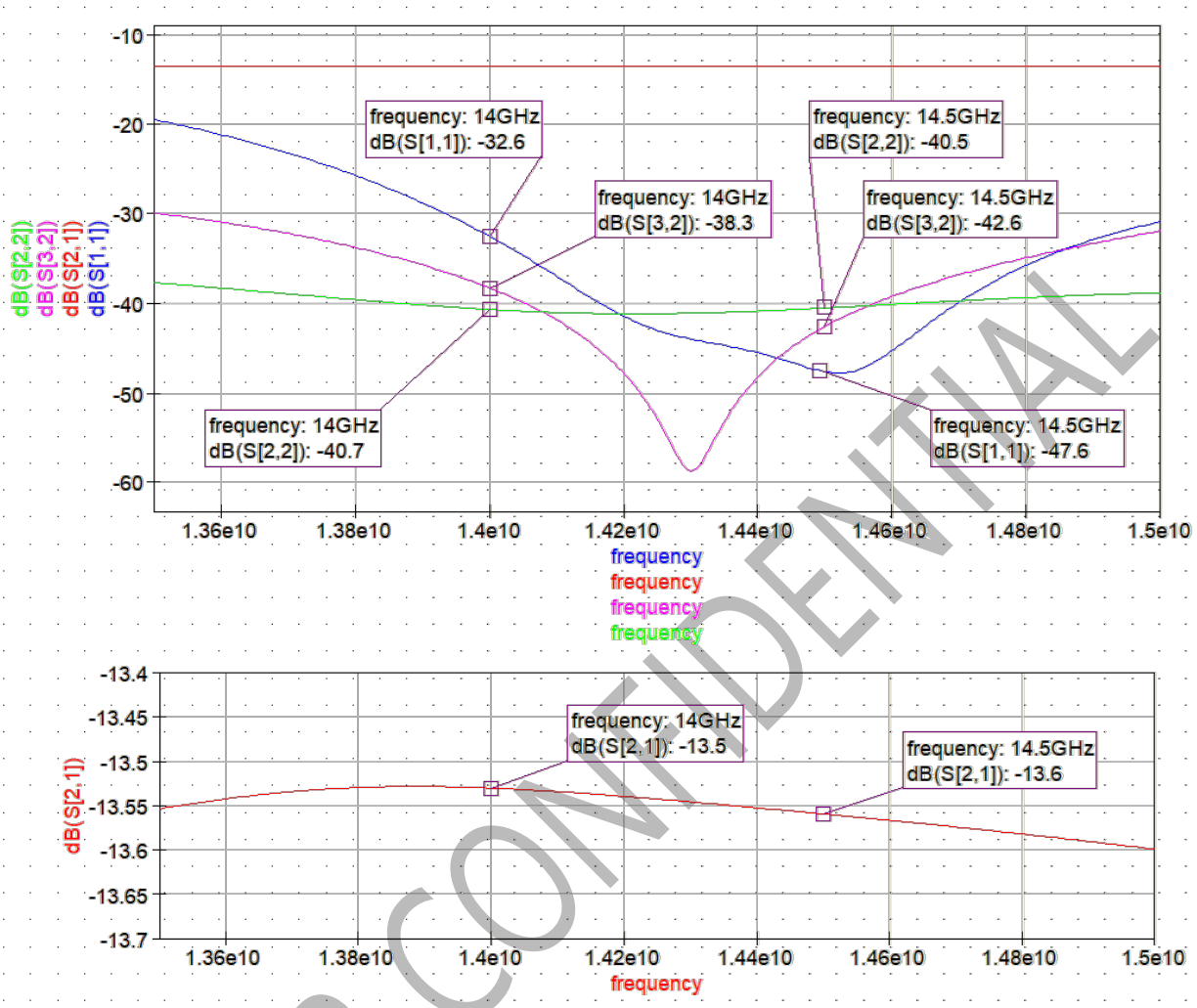

FIGURE 38: SIMULATED S-PARAMETERS OF THE TX EBBM FEEDING NETWORK

PARAMETER	VALUE
Frequency range	14.0 – 14.5 GHz
Reflection coefficient of input port	< -32.6 dB
Transmission coefficient	> -13.6 dB

TABLE 10: SIMULATED PERFORMANCE OF THE TX EBBM FEEDING NETWORK

5. Summary and Conclusions

The research and pre-design of the EBBM radiating aperture has been presented in this document. First, the topology and simulation results of the RX and TX individual radiating elements have been shown. Later, the radiating elements have been grouped using the sequential rotation technique, forming the RX and TX EBBM radiating apertures. Simulation results of these EBBM modules have been presented.

After that, the chosen combiner and splitter topology for the EBBM RF feeding networks has been presented, and the results obtained in the electromagnetic simulations have been shown. Based on the individual combiner and splitter, the reception and transmission EBBM RF feeding networks have been generated and simulated.

Following the results obtained for the EBBM radiating modules, it is expected that the grouping of these modules will allow the creation of an optimal antenna able to communicate with the emerging LEO satellite constellations. In fact, it is expected that this LEO antenna could operate in a 3GPP environment in which the NTN network is integrated into the 5G NG-RAN.

6. References

[1] Saswati Ghosh, Debarati Sen, "An Inclusive Survey on Array Antenna Design for Millimeter-Wave Communications", IEEE Access, vol. 7, pp. 83137 – 83161, 2019.

[2] I. Uchendu and J. R. Kelly, "Survey of beam steering techniques available for millimeter wave applications", Prog. Electromagn. Res. B, vol. 68, pp. 35-54, May 2016.

[3] Peter McNeil, "Analog vs. Digital Beamforming", Pasternack Blog, March 2018. https://blog.pasternack.com/antennas/analog-vs-digital-beamforming/

[4] Dr. Mohamed Nadder Hamdy, PhD, "Beamformers Explained", CommScope, 2020. https://www.commscope.com/globalassets/digizuite/542044-beamformer-explained-wp-114491-en.pdf

[5] K. Benson, "Phased Array Beamforming ICs Simplify," Analog Dialogue, p. 2, January 2019. https://www.analog.com/media/en/analog-dialogue/volume-53/number-1/phased-array-beam-forming-ics-simplify-antenna-design.pdf

[6] F. Croq and D. M. Pozar, "Millimeter-wave design of wide-band aperture-coupled stacked microstrip antennas," IEEE Trans. Antennas Propag., vol. 39, no. 12, pp. 1770– 1776, Dec 1991

[7] Constantine A. Balanis, "Antenna Theory Third Edition: Analysis and design", John Wiley & Sons, Inc., 2005.

[8] H. Parikh, S. Pandey, K. Modh, "Wideband and high gain stacked microstrip antenna for Ku band application", 2012 Nirma University International Conference on Engineering (NUiCONE), 1-5.

[9] M. Khan, Z. Yang, K. Warnick, "Dual-Circular-Polarized High-Efficiency Antenna forKu-Band Satellite Communication", IEEE Antennas and wireless propagation letters, vol. 13, 2014.

[10] B. Rohrdantz, T. Jaschke, F. K. H. Gellersen, A. Sieganschin and A. F. Jacob, "Ka-band antenna arrays with dual-frequency and dual-polarized patch elements", International Journal of Microwave and Wireless Technologies, 2016, 8(6), 963–972.

[11] Arun K. Bhattacharyya, "Phased Array Antennas", John Wiley & Sons, Inc., 2006

[12] Andrew Chrysler, Cynthia Furse, Rainee N. Simons, Félix A. Miranda, "A Ka-Band (26 GHz) Circularly Polarized 2x2 Microstrip Patch Sub-Array with Compact Feed", 2017 IEEE International Symposium on Antennas and Propagation & USNC/URSI National Radio Science Meeting, San Diego, CA, USA, July 2017.

[13] J. Huang, "A Ka-Band Circularly Polarized High-Gain Microstrip Array Antenna", IEEE Trans. Antennas and Propag., vol. 43, no. 1, pp. 113-116, Jan 1995.

[14] E.J. Wilkinson, "An N-way Power Divider", IRE Trans. on Microwave Theory and Techniques, vol. 8, p. 116-118, Jan. 1960.

[15] D.M. Pozar, Microwave Engineering, 4th Edition, John Wiley & Sons: New York, 1998, pp. 328-333.